01 Apr 2019

A Comprehensive Experimental and Modeling Study on Dissolution in Li-Ion Batteries

Yoon Koo Lee

Jonghyun Park
Missouri University of Science and Technology, parkjonghy@mst.edu

Wei Lu

Recommended Citation

A Comprehensive Experimental and Modeling Study on Dissolution in Li-Ion Batteries

Yoon Koo Lee, [1,a] Jonghyun Park, [1,*,b] and Wei Lu [1,2,z]

[1]*Department of Mechanical Engineering, University of Michigan, Ann Arbor, Michigan 48109, USA*
[2]*Department of Materials Science and Engineering, University of Michigan, Ann Arbor, Michigan 48109, USA*

Dissolution is a critical challenge in metal oxide battery materials, which affects battery performance across multiple scales. At the particle level, the loss of active material as a result of dissolution directly results in capacity fade. At the electrode level, the re-deposition of dissolved metal ions onto the cathode increases cell polarization and hinders lithium transport. At the cell level, the dissolved ions further transport to and deposit on the anode, which consumes cycle-able lithium and leads to capacity fade. These processes lead to poor lithium reversibility, diffusivity, and conductivity. In this work, detailed experimental studies from the particle level up to the cell level are systematically conducted to provide parameters for model input and model validation. A multi-physics modeling framework is developed to reveal key mechanisms associated with metal-ion dissolution and their impact on battery performance. We simulate capacity degradation during cycling and compare the results to a series of experimental data such as cyclic voltammetry, electrochemical impedance spectroscopy, and battery cycling. The integrated study have revealed several key mechanisms related to dissolution, and quantitatively connected the particle level dissolution and deposition behaviors to the cell level performance. These can provide useful guidance for battery design and management.

Rechargeable batteries that use lithium transition metal oxide systems as the cathode have been studied extensively since the past decade. In order to charge/discharge the battery by using lithium intercalation reactions, transition metal cations are needed in the lithium transition metal oxide systems. However, a major issue is that these systems often experience transition metal dissolution. Especially, batteries that use spinel $LiMn_2O_4$ as the cathode material exhibit significant capacity fade during long-term cycling or storage at elevated temperatures. Several mechanisms of capacity fade have been proposed in previous studies.[1–4] The dissolution of manganese is one of the most important causes, especially at elevated temperatures.[5–7]

Manganese dissolution can be attributed to several possible mechanisms. Manganese ions dissolve into the electrolyte when acids, generated by side reactions, attack the $LiMn_2O_4$ material. Acids such as hydrogen fluoride (HF) can be generated by two major side reactions: electrolyte oxidation and salt decomposition. Electrolyte oxidation produces hydrogen ions to form HF at voltages greater than 4.1V.[8] Salt decomposition generates hydrogen ions through the interaction of water and $LiPF_6$ salt in the electrolyte. These reactions are coupled with one another and cause capacity decrease, especially during cycling. Manganese disproportionation reactions ($2Mn^{3+} \rightarrow Mn^{4+} + Mn^{2+}$) become faster especially in the discharged state, where Mn^{2+} ions can dissolve into the electrolyte.[9] The solubility of manganese ions also increases as a result of phase transformations in high or low voltage regions during cycling.[10] As manganese ions dissolve into the electrolyte, several corresponding phenomena occur, including structural instability, the loss of active material, and an increase in ohmic resistance. All of these mechanisms are directly related to capacity fade in the $LiMn_2O_4$ electrode material.

In addition, dissolved manganese ions redeposit onto the cathode surface and generate inactive materials. While it is widely reported that dissolved manganese ions deposit on the anode side,[7,11–21] it has also been observed that they redeposit onto the cathode side and form electrically insulating oxides (Mn-O) or fluorides (Mn-F).[3,22] For example, these Mn-O and Mn-F compounds were detected, using XPS, on the surface of $LiMn_2O_4$ positive electrodes after cycling.[22] In particular, it was observed that Mn-F compounds generated during the later stage

of storage were highly resistive and led to cell polarization. These findings suggest that the manganese compounds on the cathode surface layer critically reduce the stability of spinel $LiMn_2O_4$ cathodes.[3,7,22–26] However, there is a lack of advanced research on the mechanisms of manganese redeposition and their impact on the performance of the cathode.

Several studies have used modeling and simulations to help understand the mechanisms and impacts of manganese dissolution and deposition. A mathematical model was developed to predict the capacity fade resulting from manganese ion disproportional reactions.[27] The reaction rate constant and the activation energies of manganese disproportionation reactions used in the model were obtained through experiments conducted under open circuit potential conditions using a particle electrode.[28] It was suggested that disproportional reactions cause a loss of active material as well as a decrease in effective transport properties, which lead to capacity fade. A mathematical $LiMn_2O_4$/lithium half-cell model was proposed, which considered several major side reactions including manganese dissolution from acid attacks and manganese deposition.[2] A $LiMn_2O_4$/graphite full-cell model was developed that coupled side reactions at both the cathode and the anode: the key degradation mechanisms include SEI layer formation, manganese dissolution and manganese deposition.[29] An explanation was proposed for how consecutive side reactions generate by-products, such as manganese ions, hydrogen ions and water molecules, and lead to the loss of cycleable lithium and active material.

Based on previous findings, here we expand our understanding of cathode degradation by systematically investigating a comprehensive set of parameter changes caused by dissolved manganese ions, including those that have not been well studied before. In order to study the impact of transition metal dissolution on the cell performance, we chose $LiMn_2O_4$ cathode material in this study, which has the highest dissolution rate among various transition metal oxide systems.[30] Cyclic voltammetry (CV), electrochemical impedance spectroscopy (EIS), and capacity characterization were used to assess the effect of dissolved manganese ions on the performance of the $LiMn_2O_4$ cathode. In addition, key parameters such as open circuit voltage, electronic conductivity, discharge curves, and the amount of manganese ions were measured experimentally as model inputs in an effort to provide a quantitative understanding by simulations. We considered both side reactions and the degradation of the electrode to account for the overall changes in the performance of the cathode electrode.

The most important contribution of this study is an integrated experimental and computational study that quantitatively connects the particle level manganese dissolution and deposition behaviors to the

*Electrochemical Society Member.
[a]Present address: Battery R&D, LG Chem Gwacheon R&D Center, Gyeonggi-do 13818, Korea.
[b]Present address: Department of Mechanical and Aerospace Engineering, Missouri University of Science and Technology, Rolla, Missouri 65409, USA.
[z]E-mail: weilu@umich.edu

cell level performance. In particular, this study compared the degradation of the electrode and the changes in the cell behavior using both experiments and simulations.

Experimental

Fabrication of the LiMn₂O₄ composite electrode.—The positive $LiMn_2O_4$ composite electrodes were made from stoichiometric spinel $LiMn_2O_4$ powder (Sigma-Aldrich), carbon black, and PVDF binder (Kureha KF 7208) in a mass ratio of 90:5:5. $LiMn_2O_4$ powder and carbon black were added to the PVDF binder and mixed with a Speedo Mixer (FlackTek Inc.) for 10 min. The mixed slurry (6 mil thick controlled by a doctor blade) was coated onto a 15 μm thick aluminum foil, vacuum dried at 100°C for 24 h, and then transferred into an Ar-filled glove box (MBraun) with less than 0.1 ppm of oxygen and moisture in order to avoid exposure to ambient air. The loadings of the cathode electrodes ranged from 8.68 to 11.44 mg cm⁻². With consideration of the coating thickness as well as the mass fraction and density of active material, binder and conductive additive, the calculated porosity of the electrode in our experiments was about 39 ∼ 46%. In order to minimize any variation of porosity between samples for various experiments (e.g., capacity measurement, EIS, CV), we cut small disk electrodes from the same large piece of composite electrode, so that all the electrodes used in coin cells experienced the same preparation condition.

An electrolyte volume to pore volume ratio between 2.5 and 3 is adequate in most prototype cell systems to ensure enough electrolyte,[31] where the pore volume is the sum of the calculated pore volume of the negative and positive electrodes and the pore volume of the whole separator used in the cell. The electrolyte to cathode pore volume ratio is a more direct measurement of electrolyte availability for a half-cell. It has been shown that an electrolyte to pore volume ratio of 5, or an electrolyte to cathode pore volume ratio of 12–23 for various loadings, is way more than enough to ensure consistent electrolyte availability throughout the life of the cell.[31] The electrolyte to cathode pore volume ratio was approximately 25 in our experiment, which ensured that the electrolyte was sufficiently provided in the cell.

Conductivity measurement.—The conductivity of the composite electrode was measured using the four-point probe method. Mixed slurries of composite electrode were pasted onto a non-conductive glass substrate, and then dried in vacuum at 100°C for 24 h. A four-point probe DC method was applied to the composite electrode directly on the glass substrate using a Bio-Logic VMP3 multi-channel potentiostat.

Coin cell assembly and preparation of electrolyte with Mn.— $LiMn_2O_4$ composite electrodes were assembled into sealed 2032 type coin cells (MTI) with a 0.75mm thick lithium foil (Alfa Aesar) counter and reference electrodes and a separator (Celgard 2320). In order to reduce any possible impact of manganese ions on the lithium metal, an excessive amount of lithium foil was used. In this study, we chose lithium metal instead of graphite as the anode to avoid the complication generated by a graphite anode with the presence of Mn ions. There are several previous studies about contamination of SEI layer due to Mn ions and their impact on the graphite anode. For instance, it was found that the impedance of graphite in the $LiMn_2O_4$/graphite system significantly increased even when a small amount of Mn was present in the electrolyte.[32] The impedance increase of graphite overwhelmed the impedance of the positive electrode. In addition, Mn ions have been intentionally injected in the electrolyte to observe their direct impact, which showed that Mn ions significantly affected the graphite anode.[33]

To investigate the direct impact of manganese ions on the composite electrode, the desired concentrations of manganese were dissolved in the electrolyte in advance similar to previous experiments.[33] According to the previous literature,[8,34–36] the amount of manganese dissolved from the cathode electrode has been measured under different storage and cycling conditions. The amount of manganese dissolved is affected

by the applied potential, operating temperature, charge/discharge conditions, calcination temperature, carbon content, surface area of the cathode particle, and so on.[8,34–36] Depending on the operating conditions, the amount of dissolved manganese can vary from 20 ppm[8] to 1500 ppm.[36] After 50 cycles at room temperature conditions, Jang et al. measured about 20∼60 ppm of manganese concentration after 50 cycles between 3.6V and 4.3V with differential pulse polarography.[8] The amount of manganese was also measured with different applied potentials during storage conditions (up to 1800 minutes) which measured up to 41 ppm at 4.2V. However, Xia et al. measured 1540 ppm of manganese concentration after 50 cycles between 3.5V and 4.5V at the room temperature and 7000 ppm of manganese at 50°C.[36] We carefully selected a range of manganese concentrations from 50 to 200 ppm in our study, which is a reasonable representative range of manganese concentrations according to most literatures. The target concentrations of manganese were obtained by dissolving $Mn(PF_6)_2$ at concentrations of 50, 100, 150 or 200 ppm in an electrolyte composed of 1M lithium hexafluorophosphate ($LiPF_6$, Sigma-Aldrich) in a 1:1 mixture (v/v) of ethylene carbonate (EC, Sigma-Aldrich) and dimethyl carbonate (DMC, Sigma-Aldrich). The $Mn(PF_6)_2$ salt was synthesized by reacting silver hexafluorophosphate ($AgPF_6$, Sigma-Aldrich) with the manganese chloride ($MnCl_2$, Sigma-Aldrich) in ethanol. The mixture was distilled to isolate the synthesized $Mn(PF_6)_2$. The moisture in $Mn(PF_6)_2$ was removed by heating it in a vacuum oven overnight at 90°C. Exact concentration of manganese in the electrolyte was measured by using inductively coupled plasma–optical emission spectroscopy (ICP-OES). In order to confirm that there is no additional source of supply of manganese ions, the total amount of manganese was measured for three samples after disassembly. The total amount of manganese after disassembly of the cell was very similar to the amount that was added to the electrolyte.

Electrochemical measurement.—CV, capacity, and EIS measurements were performed using a Bio-Logic VMP3 multi-channel potentiostat to measure the impact of manganese on the $LiMn_2O_4$ composite electrode. By using $LiMn_2O_4$ electrodes and different concentrations of manganese ions in the electrolyte, $LiMn_2O_4$/lithium half cells were constructed to isolate the effect of the dissolved manganese ion on the cathode.

CV was applied to the Li/$LiMn_2O_4$ composite electrode to measure redox currents and current peak changes immediately following the addition of different concentrations of manganese ions. CV was carried out at 0.5 mV/s between 3.0V and 4.5V for the Li/$LiMn_2O_4$ cell. Interfacial currents and current peak changes were measured during the formation cycles.

Capacity of the assembled Li/$LiMn_2O_4$ coin cells was measured by cycling between 3.5 V and 4.3 V with C/10 rate using the potentiostat. The Bio-Logic EC-Lab software measured and recorded the capacity and its evolution with cycle number.

EIS measurements were performed to measure impedance changes due to different concentrations of manganese ions and to different potentials of the electrode/electrolyte interface, as well as at different voltages (3.5, 3.7, 3.9, 4.1 and 4.3V) for each manganese concentration (0, 50, 100, 150 and 200 ppm) in the electrolyte. To achieve stabilized potentials before conducting EIS measurements, the cells were rested in an open circuit voltage (OCV) condition for 2 h. AC impedance spectra were obtained by applying sinusoidal waves with an amplitude of 5 mV over frequencies ranging from 100 kHz to 10 mHz.

Effective diffusion coefficient of the LiMn₂O₄ cathode.—In the low-frequency region of the EIS spectrum, we have[37]

$$-Z_{Im} = \delta\omega^{-1/2} \quad \text{and} \quad Z_{Re} = \delta\omega^{-1/2} \quad [1]$$

where δ is given by

$$\delta = \frac{V_m (dE_{ocv}/dy)}{FS\left(2D_{Li^+}^{eff}\right)^{1/2}} \quad [2]$$
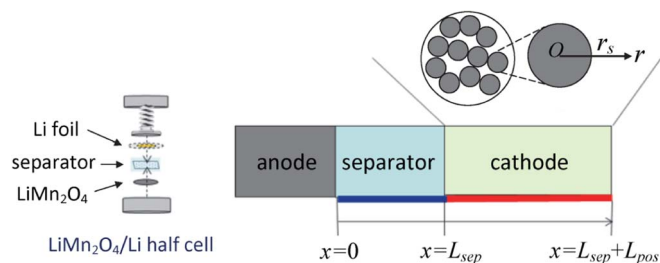
Figure 1. Configuration of the LiMn$_2$O$_4$/Li half-cell for experiment and simulation.

where Z is the Warburg impedance, ω is the angular frequency, V_m is the molar volume of the cathode, E_{ocv} is the open circuit potential, y is the intercalation level, F is Faraday's constant, S is the surface area of the electrode, and $D_{Li^+}^{eff}$ is the effective diffusion coefficient of lithium ion in the cathode. With Eq. 2, the effective diffusion coefficient of the cathode electrode can be calculated using the OCV curve, the surface area of the electrode and the EIS spectrum.

ICP-OES measurement — dissolution of manganese due to storage.—LiMn$_2$O$_4$ composite electrodes were stored in 1mL of a 1.0 M solution of LiPF$_6$ in a 1:1 (v/v) mixture of EC and DMC to measure the dissolved manganese. The positive composite electrodes were diluted and stored in centrifuge tubes at 0°C, 25°C and 40°C to observe the effect of temperature. Storage times were 1, 2, 3, 4 and 5 weeks. For each combination, five samples of ICP-OES were measured using a Perkin-Elmer Optima 2000 DV. Three samples of LiMn$_2$O$_4$ powders in a separator were also stored in 1 mL of 1.0 M LiPF$_6$ in EC: DMC (1:1, v/v) for 1 week to compare the dissolution of composite electrodes and powder.

ICP-OES measurement — dissolution due to cycling using an electrochemical cell.—The concentration of manganese in the electrolyte was measured to observe dissolution after a series of cycles. The Li/LiMn$_2$O$_4$ half-cell was made with 150μL of a 1.0M solution of LiPF$_6$ in a 1:1 (v/v) mixture of EC and DMC. Initial formation cycling was performed 5 times before the actual cycling. The C-rate for the formation cycles was C/10 and the C-rate for cycling was 1C. The LiMn$_2$O$_4$ composite electrode/lithium cell was cycled from 3.5 V to 4.3 V using a Bio-Logic VMP3 multi-channel potentiostat. After cycling, the cell was disassembled and ICP-OES measurements were conducted to measure the concentration of manganese in the electrolyte.

Model Development

The battery cell model used in this study had the same configuration as the cells used in the experimental work. These cells consisted of a LiMn$_2$O$_4$ composite electrode, lithium foil, a separator and 1M LiPF$_6$ in EC: DMC (1:1, v/v), as shown in Fig. 1. Experiments were carefully designed to investigate the degradation of the cathode material. The model included the side reactions and degradation of the cathodic side. Table I shows the parameters used in the simulations.

Side reaction modeling.—The major side reactions considered in this study are solvent oxidation, salt decomposition, hydrogen reduction, manganese dissolution, manganese deposition and manganese redeposition.

Mn dissolution.—Acid attack on the active material causes manganese dissolution. The reaction is described by[38–40]

$$4H^+ + 2LiMn_2O_4 \rightarrow 2Li^+ + Mn^{2+} + \frac{3}{2}Mn_2O_4 + 2H_2O \quad [3]$$
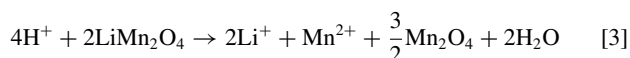
Table I. Electrode parameters.

Parameter	Value
brug, Bruggemann coefficient	1.5
$c_{1,0}$, initial concentration of lithium ions in the solid phase	6858 mol m^{-3}
$c_{1,max0}$, initial maximum solid phase concentration	22730 mol m^{-3}
$D_{1,0}$, initial diffusivity of lithium ion in solid	1.31×10^{-12} m^2 s^{-1}
D_{Li^+}, diffusivity of lithium in the electrolyte	7.51×10^{-11} m^2 s^{-1}
$f_\pm$, electrolyte activity coefficient	1
F, Faraday's constant	96487 C mol^{-1}
$k_{Li^+,0}$, initial reaction rate constant of lithium at cathode	1×10^{-5} A m$^{2.5}$ mol$^{-1.5}$
$k_{Li^+,metal}$, reaction rate constant of lithium at lithium metal anode	6.1×10^{-6} A m$^{-0.5}$ mol$^{-0.5}$
L_{pos}, cathode thickness	183×10^{-6} m
L_{sep}, separator thickness	52×10^{-6} m
κ_1^{eff}, effective solid phase electronic conductivity	9.80 S m^{-1}
R, universal gas constant	8.314 J mol^{-1} K^{-1}
t_+^0, lithium ion transference number	0.363
T, temperature	298 K
$\alpha_{a,Li}$, $\alpha_{c,Li}$ anodic and cathodic transfer coefficient of lithium intercalation/ deintercalation reaction	0.5
$\alpha_{a,Li}^{metal}$, $\alpha_{c,Li}^{metal}$ anodic and cathodic transfer coefficient at lithium metal anode	0.5
$\varepsilon_{1,0}$, initial volume fraction of electrode active material	0.297
ε_2, volume fraction of electrolyte, cathode region	0.444
ε_2, volume fraction of electrolyte, separator region	1
initial voltage	3.6 V

The reaction rate of manganese dissolution due to acid attack can be expressed as

$$R_{Mn\_dis} = k_{Mn\_dis}c_{H^+} \quad [4]$$

where k_{Mn_dis} is the reaction rate constant of Mn dissolution due to acid attack and c_{H^+} is the concentration of hydrogen ions.

Solvent oxidation.—Studies have shown that manganese dissolution is accelerated when storing the electrode at a higher voltage, compared to the dissolution rate during storage at a lower voltage.[41] It was proposed that the dependence of manganese dissolution on the potential arises from solvent oxidation on the positive electrode. Solvent decomposition generates hydrogen ions and electrons, which can be expressed as[8,39,42]

$$\text{solvent} \rightarrow \text{oxidized products} + H^+ + e^- \quad [5]$$
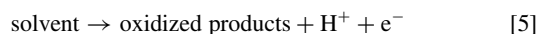
The reaction current density of solvent decomposition, i_{oxid}, which is an irreversible reaction, can be described using the Tafel equation[42]

$$i_{oxid} = i_{0,oxid} \exp\left(\frac{\alpha_{a,oxid}F}{RT}\eta_{oxid}\right) \quad [6]$$

where $i_{0,oxid}$ is the exchange current density of this side reaction, $\alpha_{a,oxid}$ is the anodic transfer coefficient of the electrolyte decomposition reaction and R is the gas constant. The overpotential of the decomposition reaction, η_{oxid}, can be described as

$$\eta_{oxid} = \phi_1 - \phi_2 - U_{oxid} \quad [7]$$

where ϕ_1 and ϕ_2 are the potentials of the solid electrode phase and the electrolyte phase, respectively, and U_{oxid} is the equilibrium potential of

the solvent oxidation reaction. The rate of the solvent decomposition reaction can be described as

$$R_{oxid} = \frac{i_{oxid}}{F} \qquad [8]$$

Salt decomposition.—Decomposition of the electrolyte, which contains the $LiPF_6$ salt, produces H^+ ions. $LiPF_6$ initially decomposes as follows

$$LiPF_6 \rightarrow LiF + PF_5 \qquad [9]$$

and then PF_5 reacts with water to form HF,

$$PF_5 + H_2O \rightarrow 2HF + POF_3 \qquad [10]$$

The rate of the $LiPF_6$ decomposition reaction, R_{decomp}, is given by[43,44]

$$R_{decomp} = k_{decomp}(c_{H_2O})^2 c_{Li^+} \qquad [11]$$

where k_{decomp} is the reaction coefficient of decomposition reaction, c_{H_2O} is the water concentration in the electrolyte, and c_{Li^+} is the lithium ion concentration in the electrolyte.

Since the concentration of PF_5 is relatively high, the water content of the cell governs the reaction rate in Eq. 10. However, water is produced by the attack of HF on the active material by the reaction in Eq. 3, therefore, manganese dissolution will accelerate continuously in the cell.

Trivalent manganese ions can disproportionate into divalent manganese ions and tetravalent manganese ions when the portion of Mn^{3+} is high.[9,30,45] While this mechanism is different from the acid attack, the impact on battery performance is similar; Mn^{2+} ions dissolve in the electrolyte and this leads to a loss of active material and additional reduction on the electrode. In this study we focus on the acid attack.

Mn deposition and H^+ reduction on anode.—On the surface of lithium foil anode ($x = 0$), Mn^{2+} and H^+ are reduced during charging, which can be expressed by

$$Mn^{2+} + 2e^- \rightarrow Mn \qquad [12]$$

$$H^+ + e^- \rightarrow \frac{1}{2}H_2 \qquad [13]$$

The reaction currents on the anode surface at $x = 0$ are given by

$$i_{Mn\_dep} = -k_{Mn\_dep}c_{Mn^{2+}} \exp\left[-\frac{\alpha_{c,Mn\_dep}F}{RT}\left(\phi_{Li\_metal} - \phi_2 - U_{Mn\_dep}\right)\right]$$
$$\text{(during charge)}$$
$$i_{Mn\_dep} = 0 \ \text{(during discharge)}$$
$$[14]$$

$$i_{H\_dep} = -k_{H\_dep}c_{H^+} \exp\left[-\frac{\alpha_{c,H\_dep}F}{RT}\left(\phi_{Li\_metal} - \phi_2 - U_{H\_dep}\right)\right]$$
$$\text{(during charge)}$$
$$i_{H\_dep} = 0 \ \text{(during discharge)}$$
$$[15]$$

The two reaction currents have a linear dependence on the concentration of the corresponding species. U_{Mn_dep} and U_{H_dep} are assumed to be constant.

Mn re-deposition on cathode.—Mn-F and Mn-O compounds have been detected, using XPS, on the surface of $LiMn_2O_4$ positive electrodes.[22] The impedance of the electrolyte/electrode interface increased dramatically when a higher concentration of manganese was added into the cell. It can be assumed that manganese ions in the electrolyte were additionally consumed during film formation on the cathode particles. Mn redeposition is controlled by a charge transfer reaction that follows the Tafel equation

$$i_{Mn\_redep} = -k_{Mn\_redep}c_{Mn^{2+}} \exp\left[-\frac{\alpha_{c,Mn\_redep}F}{RT}\left(\phi_1 - \phi_2 - U_{Mn\_redep}\right)\right]$$
$$\text{(during discharge)}$$
$$i_{Mn\_redep} = 0 \ \text{(during charge)}$$
$$[16]$$

Table II. Side reaction parameters.

Parameter	Value
$c_{H^+,0}$, initial H^+ concentration	4 mol m^{-3}
$c_{H_2O,0}$, initial H_2O concentration	4 mol m^{-3}
$c_{Mn^{2+},0}$, initial Mn^{2+} concentration	0 mol m^{-3}
D_{H^+}, diffusivity of H^+	5×10^{-9} m^2 s^{-1}
D_{H_2O}, diffusivity of H_2O	3×10^{-9} m^2 s^{-1}
$D_{Mn^{2+}}$, diffusivity of Mn^{2+}	0.72×10^{-9} m^2 s^{-1}
$a_{s,oxid}i_{0,oxid}$, current of solvent oxidation	10 A m^{-3}
k_{decomp}, reaction rate constant of salt decomposition	7.13×10^{-10} m^6 mol^{-2} s^{-1}
k_{H_dep}, reaction rate constant of hydrogen deposition	3.07×10^{-8} A m mol^{-1}
k_{Mn_dep}, reaction rate constant of Mn deposition	1.3×10^{-9} A m mol^{-1}
k_{Mn_dis}, reaction rate constant of Mn dissolution	4.1×10^{-12} m s^{-1}
k_{Mn_redep}, reaction rate constant of Mn re-deposition	1.3×10^{-9} A m mol^{-1}
n_1, adjustment factor of lithium diffusivity	0.12
U_{H_dep}, equilibrium potential of hydrogen deposition	2.5 V
U_{Mn_dep}, equilibrium potential of Mn deposition	1.5 V
U_{oxid}, equilibrium potential of solvent oxidation	4.2 V
$\alpha_{a,oxid}$, anodic transfer coefficient of solvent oxidation	0.01
α_{c,H_dep}, cathodic transfer coefficient of hydrogen deposition	0.5
α_{c,Mn_dep}, cathodic transfer coefficient of Mn deposition	0.5

The rate of Mn redeposition is given by

$$R_{Mn\_redep} = -\frac{i_{Mn\_redep}}{F} \qquad [17]$$

Table II summarizes the side reaction parameters used in the simulations.

Cell level modeling.—The model consists of 8 partial different equations that were coupled and solved simultaneously to describe the reaction mechanisms at the cathode:

(a) 2 charge conservation equations for Li^+ in the cathode and in the electrolyte.
(b) 4 equations describing the transport of Li^+, Mn^{2+}, H^+ and H_2O in the electrolyte.
(c) 1 equation describing the transport of Li^+ in the cathode.
(d) 1 equation describing the change in the volume fraction of the active material in the cathode due to manganese dissolution (see next section: *Degradation of cathode material*)

Charge conservation.—Charge conservation in the cathode and in the electrolyte can be described by

$$\frac{\partial}{\partial x}\left(\kappa_1^{eff}\frac{\partial \phi_1}{\partial x}\right) - a_s i_{tot} = 0 \qquad [18]$$

$$\frac{\partial}{\partial x}\left(\kappa_2^{eff}\left(\frac{\partial \phi_2}{\partial x} - \frac{2RT}{F}\left(1 - t_+^0\right)\left(1 + \frac{d\ln f_\pm}{d\ln c_{Li^+}}\right)\frac{\partial \ln c_{Li^+}}{\partial x}\right)\right)$$
$$+ a_s i_{tot} = 0 \qquad [19]$$

The meaning of symbols is listed at the end of this paper. In the separator region ($0 < x < L_{sep}$) Eq. 19 applies with $i_{tot} = 0$. In the cathode (positive electrode) region ($L_{sep} < x < L_{sep} + L_{pos}$) Eq. 18 and Eq. 19 apply. The corresponding porosity of the separator and of the cathode is used in each region, respectively.

Lithium intercalation/deintercalation reactions on the cathode are governed by the Butler-Volmer equation

$$i_{Li^+} = i_{0,Li^+} \left[\exp\left(\frac{\alpha_{a,Li} F}{RT} \eta_{Li^+} \right) - \exp\left(-\frac{\alpha_{c,Li} F}{RT} \eta_{Li^+} \right) \right] \quad [20]$$

where i_{0,Li^+} is the exchange current of lithium intercalation/deintercalation reactions, given by

$$i_{0,Li^+} = k_{Li^+} c_{1,surf}^{0.5} \left(c_{1,max} - c_{1,surf} \right)^{0.5} c_{Li^+}^{0.5} \quad [21]$$

where k_{Li^+} is the reaction rate constant in the positive electrode, $c_{1,max}$ is the maximum concentration of lithium ion in the cathode particles, and $c_{1,surf}$ is the concentration of lithium ions on the surface of cathode particles. The expression of overpotential for lithium intercalation/deintercalation, η_{Li^+}, will be given later.

The total local transfer current density is given by

$$i_{tot} = i_{Li^+} + \frac{a_{s,oxid}}{a_s} i_{oxid} + i_{Mn\_redep} \quad [22]$$

The current density is carried entirely by the electrolyte phase at the interface between the separator and the cathode, giving the boundary condition

$$-\kappa_1^{eff} \frac{\partial \phi_1}{\partial x} \bigg|_{x=L_{sep}} = 0 \quad [23]$$

The current density is carried entirely by the solid phase at the right end of the cathode, giving

$$-\kappa_1^{eff} \frac{\partial \phi_1}{\partial x} \bigg|_{x=L_{sep}+L_{pos}} = I_{app} \quad [24]$$

where I_{app} is the applied current density and is defined positive when the battery discharges, i.e., when lithium ions flow from the anode to the cathode in the cell.

The lithium current density on the anode surface is given by

$$i_{Li^+,metal} = k_{Li^+,metal} c_{Li^+}^{0.5} \left[\exp\left(\frac{\alpha_{a,Li}^{metal} F}{RT} \left(\phi_{Li\_metal} - \phi_2 \right) \right) - \exp\left(-\frac{\alpha_{c,Li}^{metal} F}{RT} \left(\phi_{Li\_metal} - \phi_2 \right) \right) \right] \quad [25]$$

The potential at the anode surface is set to zero.

$$\phi_{Li\_metal} \big|_{x=0} = 0 \quad [26]$$

The total reaction current density on the anode surface gives a boundary condition for ϕ_2 at $x = 0$ in terms of

$$i_{Li^+,metal} + i_{Mn\_dep} + i_{H\_dep} = I_{app} \quad [27]$$

The other boundary condition for the electrolyte phase can be expressed as

$$-\kappa_2^{eff} \frac{\partial \phi_2}{\partial x} \bigg|_{x=L_{sep}+L_{pos}} = 0 \quad [28]$$

The current density in the electrolyte phase is continuous across the interface between the separator and the cathode regions.

Mass transport.—The transport equations of Li^+, Mn^{2+}, H^+ and H_2O have different forms in the separator and in the cathode regions. In the following, we consider these two regions separately.

Separator region $(0 < x < L_{sep})$

In the separator region only electrolyte decomposition occurs as the side reaction. The transport equations of the species are given by

$$\varepsilon_2 \frac{\partial c_{Li^+}}{\partial t} = \frac{\partial}{\partial x} \left(D_{Li^+}^{eff} \frac{\partial c_{Li^+}}{\partial x} \right) - R_{decomp} \quad [29]$$

$$\varepsilon_2 \frac{\partial c_{Mn^{2+}}}{\partial t} = \frac{\partial}{\partial x} \left(D_{Mn^{2+}}^{eff} \frac{\partial c_{Mn^{2+}}}{\partial x} \right) \quad [30]$$

$$\varepsilon_2 \frac{\partial c_{H^+}}{\partial t} = \frac{\partial}{\partial x} \left(D_{H^+}^{eff} \frac{\partial c_{H^+}}{\partial x} \right) + 2R_{decomp} \quad [31]$$

$$\varepsilon_2 \frac{\partial c_{H_2O}}{\partial t} = \frac{\partial}{\partial x} \left(D_{H_2O}^{eff} \frac{\partial c_{H_2O}}{\partial x} \right) - R_{decomp} \quad [32]$$

Note that the concentration of Li^+ (1000 mM $LiPF_6$) is significantly higher than the concentrations of Mn^{2+} (1.016 mM after 50 cycles, from experiment results) and H^+ (less than 50 ppm). Therefore, the contributions of Mn^{2+} and H^+ to the electric field in the electrolyte can be neglected. The boundary conditions for the four species on the anode surface are given by

$$-D_{Li^+}^{eff} \frac{\partial c_{Li^+}}{\partial x} \bigg|_{x=0} = \frac{1 - t_+^0}{F} i_{Li^+,metal} \quad [33]$$

$$-D_{Mn^{2+}}^{eff} \frac{\partial c_{Mn^{2+}}}{\partial x} \bigg|_{x=0} = \frac{i_{Mn\_dep}}{F} \quad [34]$$

$$-D_{H^+}^{eff} \frac{\partial c_{H^+}}{\partial x} \bigg|_{x=0} = \frac{i_{H\_dep}}{F} \quad [35]$$

$$\frac{\partial c_{H_2O}}{\partial x} \bigg|_{x=0} = 0 \quad [36]$$

The flux of the four species are continues across the interface between the separator and the cathode regions, given by

$$-D_{Li^+}^{eff} \frac{\partial c_{Li^+}}{\partial x} \bigg|_{x=L_{sep}^-} = -D_{Li^+}^{eff} \frac{\partial c_{Li^+}}{\partial x} \bigg|_{x=L_{sep}^+} \quad [37]$$

$$-D_{Mn^{2+}}^{eff} \frac{\partial c_{Mn^{2+}}}{\partial x} \bigg|_{x=L_{sep}^-} = -D_{Mn^{2+}}^{eff} \frac{\partial c_{Mn^{2+}}}{\partial x} \bigg|_{x=L_{sep}^+} \quad [38]$$

$$-D_{H^+}^{eff} \frac{\partial c_{H^+}}{\partial x} \bigg|_{x=L_{sep}^-} = -D_{H^+}^{eff} \frac{\partial c_{H^+}}{\partial x} \bigg|_{x=L_{sep}^+} \quad [39]$$

$$-D_{H_2O}^{eff} \frac{\partial c_{H_2O}}{\partial x} \bigg|_{x=L_{sep}^-} = -D_{H_2O}^{eff} \frac{\partial c_{H_2O}}{\partial x} \bigg|_{x=L_{sep}^+} \quad [40]$$

In the above equations the material parameters and concentrated fields in the separator region next to the separator/cathode interface ($x = L_{sep}^-$) and in the cathode region next to the separator/cathode interface ($x = L_{sep}^+$) are used, respectively.

Cathode region $(L_{sep} < x < L_{sep} + L_{pos})$

The material balance equations are

$$\varepsilon_2 \frac{\partial c_{Li^+}}{\partial t} = \frac{\partial}{\partial x} \left(D_{Li^+}^{eff} \frac{\partial c_{Li^+}}{\partial x} \right) + \frac{1 - t_+^0}{F} a_s i_{Li^+} - R_{decomp} + 2a_s R_{Mn\_dis} \quad [41]$$

$$\varepsilon_2 \frac{\partial c_{Mn^{2+}}}{\partial t} = \frac{\partial}{\partial x} \left(D_{Mn^{2+}}^{eff} \frac{\partial c_{Mn^{2+}}}{\partial x} \right) + a_s R_{Mn\_dis} - a_s R_{Mn\_redep} \quad [42]$$

$$\varepsilon_2 \frac{\partial c_{H^+}}{\partial t} = \frac{\partial}{\partial x} \left(D_{H^+}^{eff} \frac{\partial c_{H^+}}{\partial x} \right) + 2R_{decomp} + a_{s,oxide} R_{oxide} - 4a_s R_{Mn\_dis} \quad [43]$$

$$\varepsilon_2 \frac{\partial c_{H_2O}}{\partial t} = \frac{\partial}{\partial x} \left(D_{H_2O}^{eff} \frac{\partial c_{H_2O}}{\partial x} \right) - R_{decomp} + 2a_s R_{Mn\_dis} \quad [44]$$

The boundary conditions for the species at $x = L_{sep} + L_{pos}$ are

$$\frac{\partial c_{Li^+}}{\partial x}\bigg|_{x=L_{sep}+L_{pos}} = 0 \qquad [45]$$

$$\frac{\partial c_{Mn^{2+}}}{\partial x}\bigg|_{x=L_{sep}+L_{pos}} = 0 \qquad [46]$$

$$\frac{\partial c_{H^+}}{\partial x}\bigg|_{x=L_{sep}+L_{pos}} = 0 \qquad [47]$$

$$\frac{\partial c_{H_2O}}{\partial x}\bigg|_{x=L_{sep}+L_{pos}} = 0 \qquad [48]$$

In the solid particles of the cathode, the material transport is given by

$$\frac{\partial c_1}{\partial t} = \frac{D_1}{r^2}\frac{\partial}{\partial r}\left(r^2\frac{\partial c_1}{\partial r}\right) \qquad [49]$$

The boundary conditions for solid phase diffusion can be expressed as

$$-D_1\frac{\partial c_1}{\partial r}\bigg|_{r=0} = 0 \qquad [50]$$

$$-D_1\frac{\partial c_1}{\partial r}\bigg|_{r=r_s} = \frac{i_{Li^+}}{F} \qquad [51]$$

Degradation of cathode material.—The cell level model is affected by the cathode material degradation through several mechanisms.

Loss of active material.—Mn dissolution reduces the effective volume fraction of the solid phase. This effect can be expressed as

$$\frac{\partial \varepsilon_1}{\partial t} = -a_s R_{Mn\_dis} V_{LMO} = -a_s k_{Mn\_dis} c_{H^+} V_{LMO} \qquad [52]$$

where V_{LMO} is the molar volume of the cathode $LiMn_2O_4$ material. The initial volume fraction at $t = 0$ is noted as $\varepsilon_{1,0}$. An integration gives the volume fraction at time t.

The rate constant for manganese dissolution can be experimentally determined by measuring the amount of manganese dissolved from the cathode material with time. The concentration of manganese was measured by ICP-OES. With Eqs. 4 and 42, and considering that the amount of re-deposited Mn onto the cathode is negligible, the rate of manganese dissolution, k_{Mn_dis}, was estimated using

$$\varepsilon_2 \frac{\partial c_{Mn^{2+}}}{\partial t} = a_s k_{Mn\_dis} c_{H^+} \qquad [53]$$

The maximum solid phase concentration decreases proportionally to the volume fraction of the electrode, giving

$$c_{1,max} = c_{1,max0}\frac{\varepsilon_1}{\varepsilon_{1,0}} \qquad [54]$$

The specific surface area of the cathode also decreases as the Mn dissolution occurs, which is given by

$$a_s = \frac{3\varepsilon_1}{r_s} \qquad [55]$$

Increase of resistance.—By separating the frequency regions of the EIS spectra, reactions and electrochemical characteristics of the electrode and electrolyte can be identified,[46–49] allowing quantification of ohmic resistance, charge transfer resistance and lithium diffusion. ohmic resistance is mainly related to the immediate voltage drop caused by pure ohmic resistance of the electrode. The voltage decreases further due to changes in the lithium concentration at the surface of active particles, which causes a change in the electromotive force that relates to the charge transfer resistance.[49] In this paper, the effect of ohmic resistance is reflected in the overpotential for lithium intercalation/deintercalation, while the effect of charge transfer resistance change is included by changing the reaction rate coefficient of positive electrode. The diffusion coefficient, ohmic resistance and reaction rate coefficient as functions of Mn concentration were used as input to the simulation.

Ohmic resistance.—The ohmic resistance between the cathode and the electrolyte increases with cycling as a result of redeposited manganese compounds and film formation on the cathode surface. It affects the overpotential for lithium intercalation/deintercalation, giving

$$\eta_{Li^+} = \phi_1 - \phi_2 - U_{Li^+} - i_{Li^+}R_{ohmic} \qquad [56]$$

where R_{ohmic} is the ohmic resistance.

The importance of film resistance on cell performance was noted in several works.[50–52] By measuring the interfacial resistance of the electrode at several pre-dissolved manganese concentrations (0, 50, 100, 150 and 200 ppm), we were able to determine the resistance at any manganese concentration using linear interpolation.

Charge transfer resistance.—The ability to transfer lithium ions at the electrode/electrolyte interface decreases and the charge transfer reaction slows down with manganese ions in the electrolyte. The interfacial resistance at the cathode/electrolyte interface has been proposed to be[53,54]

$$R_{ct} = \frac{RT}{i_{0,Li^+}F} = \frac{RT}{Fk_{Li^+}c_{1,surf}^{0.5}\left(c_{1,max} - c_{1,surf}\right)^{0.5}c_{Li^+}^{0.5}}$$

$$= \frac{RT}{Fk_{Li^+}c_{1,max}c_{Li^+}^{0.5}y^{0.5}(1-y)^{0.5}} \qquad [57]$$

where $y = c_{1,surf}/c_{1,max}$ is the intercalation level.

In order to evaluate the effect of manganese ions on cell performance, the change of reaction rate constants is considered in the simulation. This requires measuring charge transfer resistance by using an experiment at the same voltage. Similar as the case of ohmic resistance, the charge transfer resistance at representative manganese concentrations was obtained experimentally. Interpolation was then used to give the charge transfer resistance at any concentration of manganese ions.

Decrease of diffusion coefficient.—The effective diffusion coefficient of the cathode electrode can be calculated using the OCV curve, the surface area of the electrode and the EIS spectrum using Eq. 2. As Mn re-deposition occurs on the cathode surface, the effective diffusion coefficient in the solid decreases because the pores in the cathode material become clogged.[2,55,56] This effect is described by

$$D_1 = D_{1,0}\left[1 - \left(\frac{\varepsilon_{1,0} - \varepsilon_1}{\varepsilon_{1,0}}\right)^{n_1}\right] \qquad [58]$$

where $D_{1,0}$ is the initial diffusion coefficient measured using EIS at different concentrations of Mn in Table V and n_1 is an adjustment factor.

The effective diffusion coefficient of Li^+, Mn^{2+}, H^+ and H_2O in the electrolyte depend on porosity, which can be described as
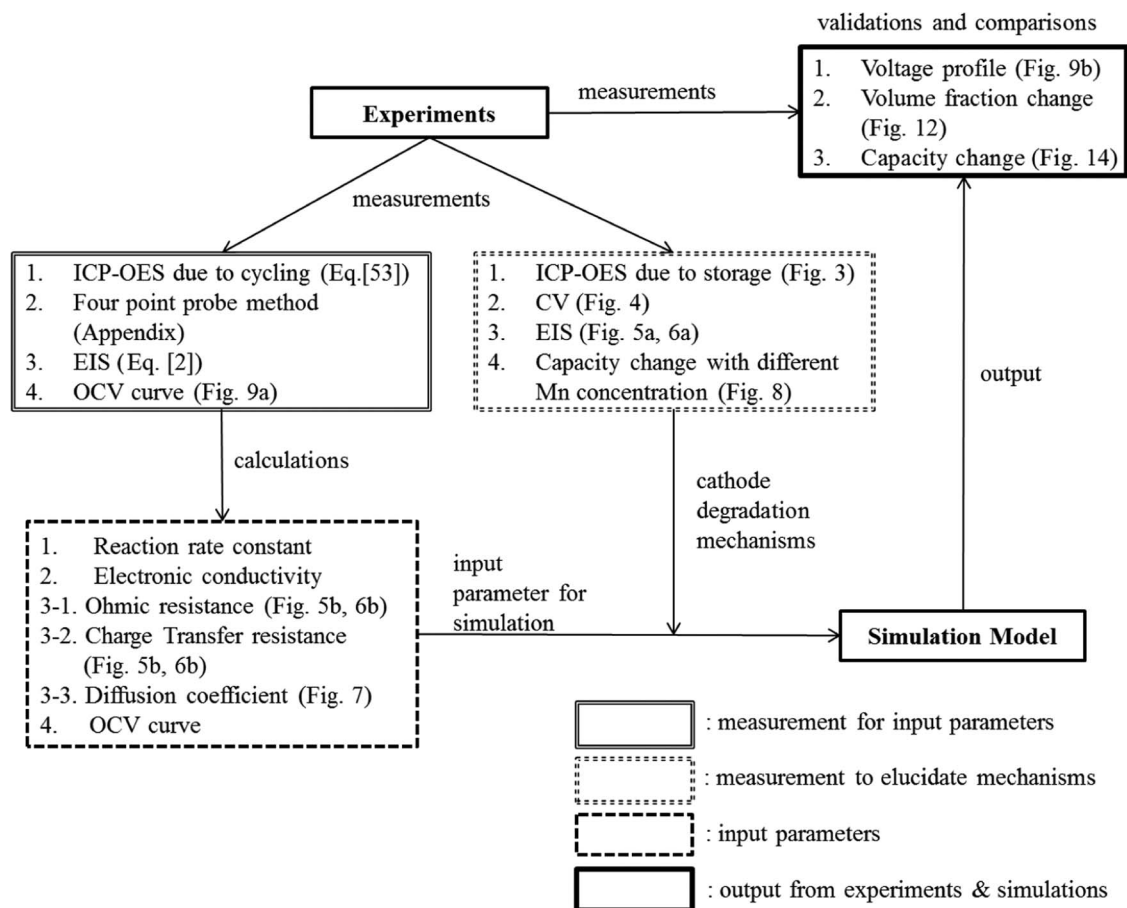
$$D_i^{eff} = D_i\varepsilon_2^{brug}\ (i = Li^+,\ H^+,\ Mn^{2+},\ H_2O) \qquad [59]$$

where D_i stands for the diffusion coefficient of the species in the bulk electrolyte and brug is the Bruggeman number.

Similarly, the effective conductivity of Li^+ in the electrolyte is given by

$$\kappa_2^{eff} = \kappa_2\varepsilon_2^{brug} \qquad [60]$$

where κ_2 is the conductivity of Li^+ in the bulk electrolyte.

Figure 2. Schematic diagram to bridge experiment and modeling.

Results and Discussion

Multiple experimental techniques were used to understand the degradation of the cathode due to manganese ions and to provide input parameters for simulations. By performing simulations using a physics-based degradation model and input parameters from measurements, we were able to directly compare the outputs of simulations and experiments for validation. Fig. 2 shows the schematic diagram to bridge experiments and simulations. In this study, several experiments were performed. Some were carried out to understand the degradation mechanisms, some were used as input parameters for simulations, while others were used for validation of model predictions. In order to distinguish the purpose of experiments, different types of boxes were used in Fig. 2. In addition, inputs, outputs, experimental techniques and relevant equations, and connection to figures of simulation results are shown.

Conductivity measurements.—The electrical resistance of a cell comes from the resistance of electrode particles, conductive additives, percolation networks in the electrode, current collectors, and the electrical tap.[50,57–59] The electronic conductivity of pure $LiMn_2O_4$ is about 0.2 $\times 10^{-6} - 2 \times 10^{-6}$ S m^{-1}, while the conductivity of a composite electrode is highly dependent on the amount of carbon black in the sample.[2,56,59] We used the measured value of 9.8 S m^{-1} as the input parameter for the effective solid phase electronic conductivity, κ_1^{eff}, in the simulation.

ICP-OES measurements.—Manganese dissolution is coupled with other side reactions, such as electrolyte oxidation. Manganese deposition onto both the cathode and anode degrades cell performance. Moreover, the amount of manganese dissolved from the $LiMn_2O_4$ spinel electrode is greatly affected by many other parameters, including temperature, operating voltage, electrolyte, salt, particle size, and C-rate,

which makes the reaction even more complicated. To accurately predict the change in cell performance due to these side reactions, the precise amount of dissolved manganese must be determined.

To understand the effects of temperature, storage time, and particle size on manganese dissolution, the amount of manganese dissolved from the positive electrode was measured using ICP-OES. Table III shows the concentration of manganese dissolved from a $LiMn_2O_4$ composite electrode during storage in 1 M $LiPF_6$ EC: DMC (1:1) electrolyte for 1 week to 5 weeks at 0°C, room temperature, and 40°C. In the table, the Mn dissolution (mM) is obtained by dividing the measured ppm value of Mn concentration in the electrolyte (mg l^{-1}) by the molar mass of Mn (54.938 g mol^{-1}). The results show that high temperature and extended storage time accelerate the dissolution process. For example, manganese in a porous electrode dissolves 31 times faster at 40°C than at room temperature after 3 weeks.

Fig. 3 shows the average concentration of manganese dissolved from a composite electrode and a particle powder electrode with

Table III. Concentration of dissolved manganese from $LiMn_2O_4$ composite electrode during storage in 1 M LiPF6 EC:DMC (1:1) electrolyte.

| Storage time	Dissolved Mn concentration (ppm)		
	0°C	RT	40°C
1 week	0.089 (1.620 μM)	0.121 (2.202 μM)	0.864 (0.0157 mM)
2 week	0.158 (2.876 μM)	0.163 (2.967 μM)	3.26 (0.0593 mM)
3 week	0.131 (2.385 μM)	0.169 (3.076 μM)	5.27 (0.0959 mM)
4 week	0.133 (2.421 μM)	0.229 (4.168 μM)	7.87 (0.143 mM)
5 week	0.225 (4.096 μM)	0.298 (5.424 μM)	19.5 (0.355 mM)
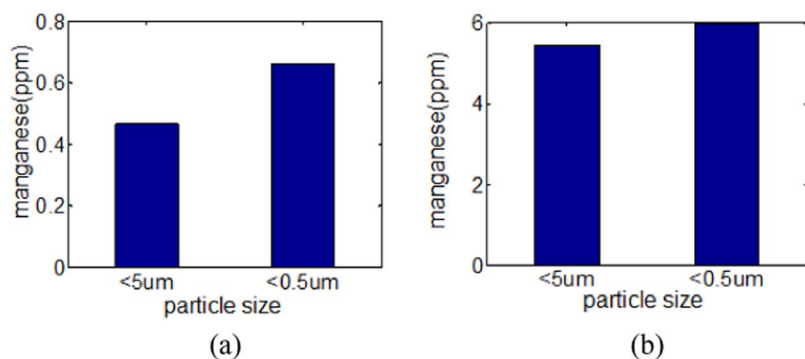
Figure 3. Concentration of dissolved manganese after 7 days from (a) composite electrode and from (b) particle powder electrode, in 1M LiPF$_6$ in EC:DMC (1:1).

different particle sizes, after storage for 7 days. Electrodes with smaller particle size tend to dissolve faster than electrodes with larger particle size for both powder and composite electrodes. This is because the electrodes with smaller particle size have larger surface area exposed to the electrolyte, leading to more acid attack. The manganese concentration as a result of dissolution from the powder electrode was about 10 times higher than that from the composite electrode. This was resulted from the larger surface area in contact with the electrolyte in the powder electrode, which may be caused in part by the PVDF binder used in the composite electrode. PVDF binder provides good adhesion for bonding between particles and between particles and the current collector, which may reduce the surface area of active material exposed to the electrolyte, resulting in decrease in manganese dissolution.

Table IV shows the concentration of dissolved manganese from the composite electrodes with particle size of 5 μm in 1 M LiPF$_6$ in EC:DMC (1:1) after different number of cycles. Three formation cycles were performed with C/10 before the actual cycles. Cycling the cell causes more manganese ions to dissolve from the LiMn$_2$O$_4$ electrode than storing the electrode in the electrolyte. A previous study that used the rotating ring disk electrode method showed that 16.5 ppm (0.3 mM) of manganese dissolved after 50 cycles.[35] Another study reported that 60 ppm (1.092 mM) of manganese dissolved after 55 cycles.[60] In this study, 1.017 mM of manganese dissolved after 50 cycle, which falls within the range observed in previous studies.

CV and EIS measurements.—Fig. 4 shows the results of CV measurement of LiMn$_2$O$_4$ electrodes with different concentration of manganese in the electrolyte. Increasing the concentration of manganese to 200 ppm caused a 5.37% decrease in the cathodic current peak of the LiMn$_2$O$_4$ electrode. The ability to transfer currents between electrolyte/electrode interfaces decreased as a result of manganese ions. Fig. 5a shows the EIS spectra of LiMn$_2$O$_4$ electrodes at different voltage. By using EIS, we can separate the sources of impedance such as the electrolyte, the SEI layer, the interface, and diffusion through the LiMn$_2$O$_4$ electrode. Typical impedance spectra for a composite electrode is composed of a semicircle with an inclined slope, as can be seen in Fig. 5. The left end point of the semicircle in the higher frequency domain relates to the ohmic resistance of the electrolyte within the separator, while the radius of the semicircle in the mid-range frequency zone relates to the charge-transfer reaction at the electrolyte/electrode interface. The inclined line connected to the semicircle on the right indicates the diffusion of lithium into the electrode. We

adopted a model from the previous literature[49] to quantify the ohmic resistance and charge transfer resistance. This model contains an element composed of a resistor (charge-transfer resistance) and a capacitor (double layer capacitance) connected in parallel. This element is further connected to a resistor (ohmic resistance) in serial. The EIS spectra in Fig. 5 were fitted by using the Bio-Logic EC-Lab software to extract the ohmic resistance and charge-transfer resistance shown in Fig. 6.

(a)

(b)
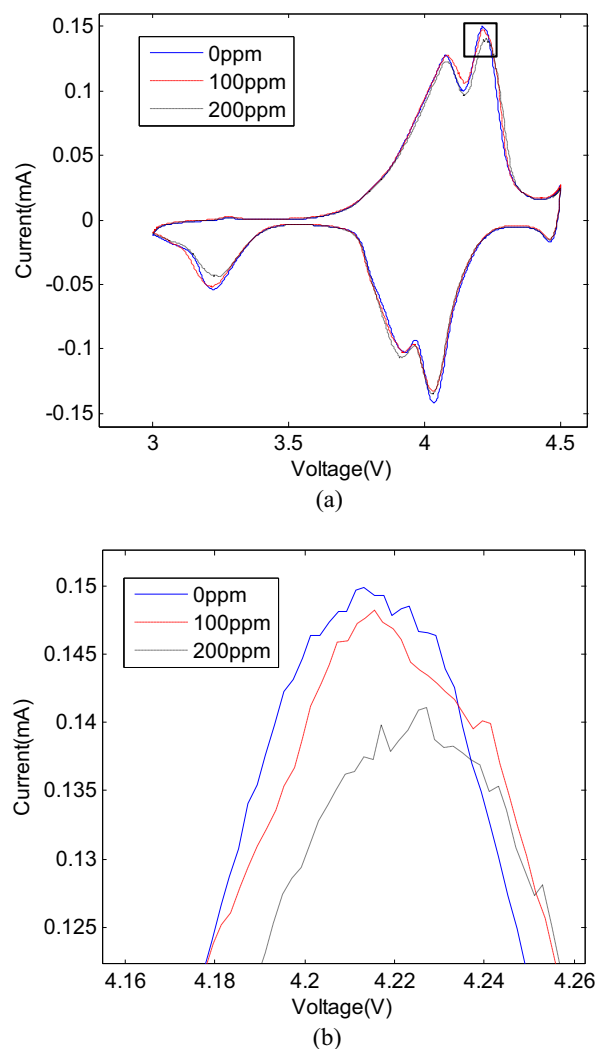
Figure 4. (a) CV curves of LiMn$_2$O$_4$ electrodes with different concentration of manganese in the electrolyte. (b) Magnified view of the high current area near 4.2V (the box region in (a)).

Table IV. Concentration of dissolved manganese from LiMn$_2$O$_4$ composite electrodes in 1 M LiPF$_6$ in EC:DMC (1:1) after different number of cycles.
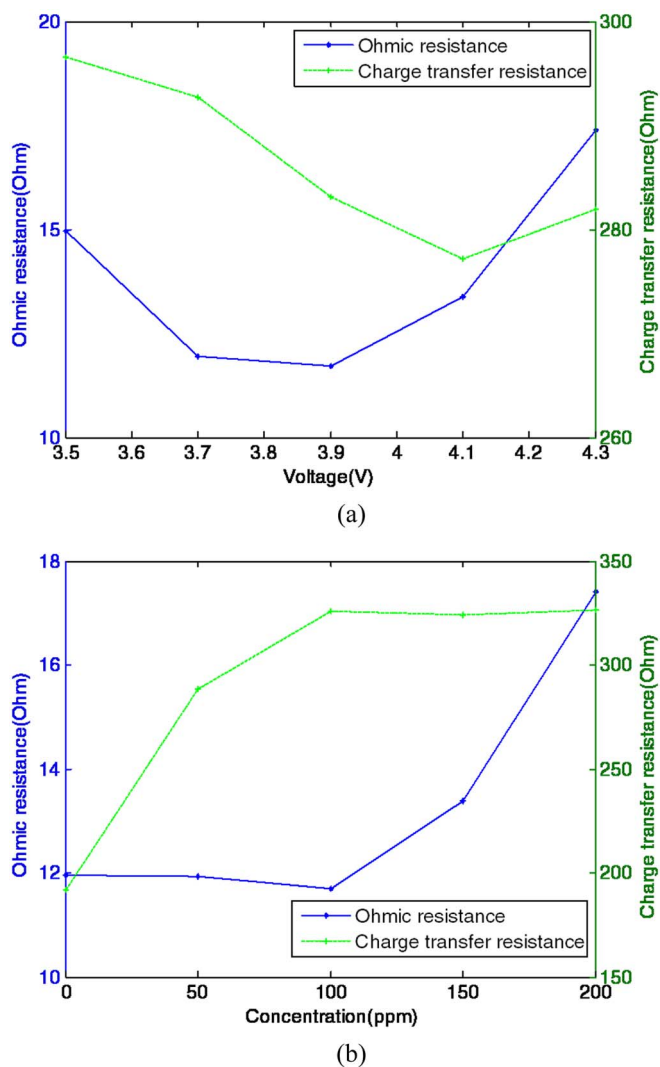
Number of cycles	Dissolved Mn concentration (ppm)
15	9.79 (0.178 mM)
30	13.53 (0.246 mM)
50	55.88 (1.017 mM)
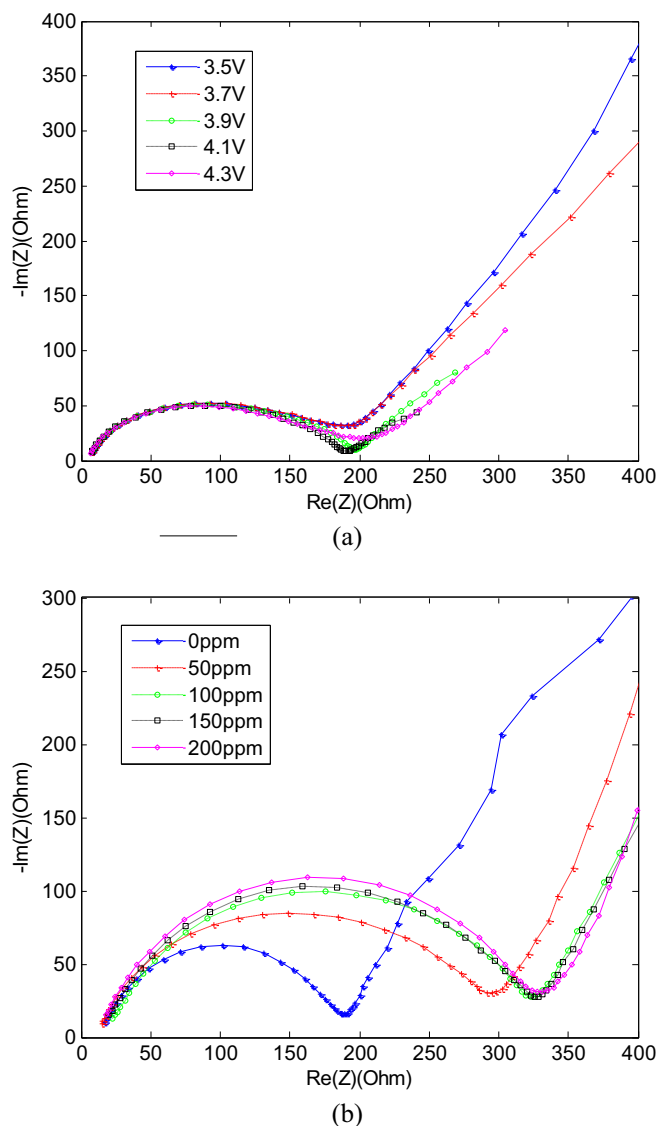
Figure 5. (a) EIS spectra of LiMn$_2$O$_4$ electrodes at different voltage. (b) EIS spectra of LiMn$_2$O$_4$ electrodes with different manganese concentration in the electrolyte.
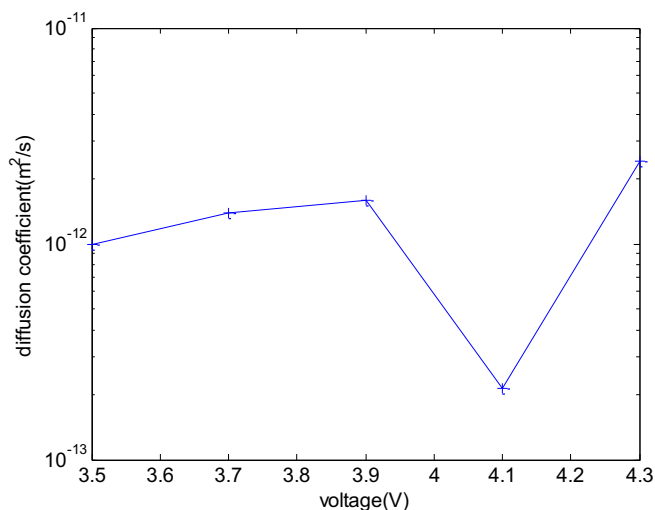

Figure 6. Ohmic resistance and charge-transfer resistance as (a) a function of voltage and (b) a function of manganese concentration in the electrolyte.
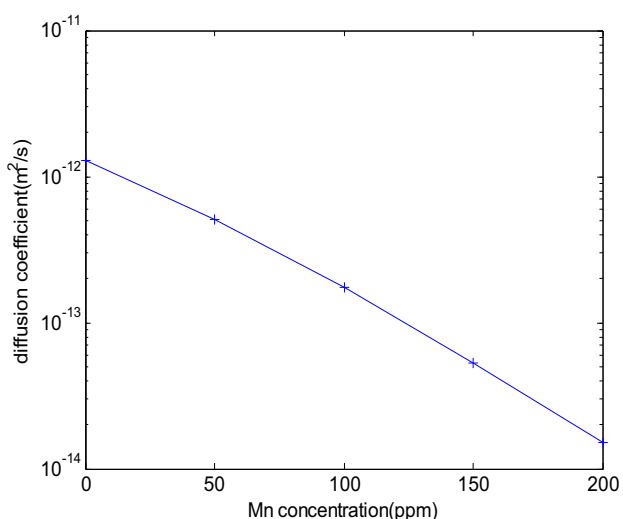
Ohmic resistance and charge-transfer resistance were plotted separately to observe the effect of voltage, as shown in Fig. 6a. The change in charge transfer resistance is related to lithium concentration in the electrode, and its dependence on voltage follows Eq. 57. This equation predicts a decrease of charge transfer resistance with y when $y < 0.5$, and an increase of charge transfer resistance with y when $y > 0.5$. The minimum charge transfer resistance is reached at $y = 0.5$ in the Li$_y$Mn$_2$O$_4$ electrode. This is consistent with our experimental data. In Fig. 6a, the lowest charge transfer resistance occurs at 4.1V, which is known to correspond to an intercalation level of $y = 0.5$ for the Li$_y$Mn$_2$O$_4$ material.

Fig. 5b shows the EIS response of the LiMn$_2$O$_4$ electrode with different manganese concentration in the electrolyte. Fig. 6b plots the ohmic resistance and charge-transfer resistance separately to show the impact of manganese. As expected, both ohmic and charge transfer resistance increased with higher concentration of manganese. The ohmic resistance of LiMn$_2$O$_4$ electrodes increased due to the additional layer formation induced by manganese re-deposition. Charge-transfer resistance also increased remarkably in LiMn$_2$O$_4$ electrodes due to the manganese ions in the electrolyte. These increases are probably caused by the Mn-F and Mn-O compounds, which are generated due to Mn re-deposition on the cathode and are highly resistive. Their formation leads to cell polarization and hinders the charge transfer process.[22]

Fig. 7 shows the effective diffusion coefficient of Li in the LiMn$_2$O$_4$ composite electrode as a function of voltage and manganese concentration from the EIS measurement. This value varied from 10^{-8} to 10^{-12} m^2 s in existing studies, depending on the measurement technique and experimental conditions.[60] Since the diffusion coefficient varies dramatically depending on the specific cell condition, it is important to measure the value of the lab-made cell to compare between experiments and simulations. The diffusion coefficient has a dependence on voltage, as shown in Fig. 7a. The voltage changes during cycling. For simplicity, the average value of the diffusion coefficient was used as input to the simulation.

The diffusion coefficient of LiMn$_2$O$_4$ electrodes was also measured after adding different concentration of manganese in the electrolyte, as shown in Fig. 7b and Table V. Manganese ions in the electrolyte substantially decrease the diffusion of lithium into the electrode. After adding 200 ppm manganese to the electrolyte, the diffusion coefficient dropped from 1.3×10^{-12} m^2 s^{-1} to 1.51×10^{-14} m^2 s^{-1}. Dissolved manganese and electrolyte decomposition products generate additional inactive film growth, as reflected by the increase in ohmic resistance and charge transfer resistance. This blocks lithium ion transport to the electrode.
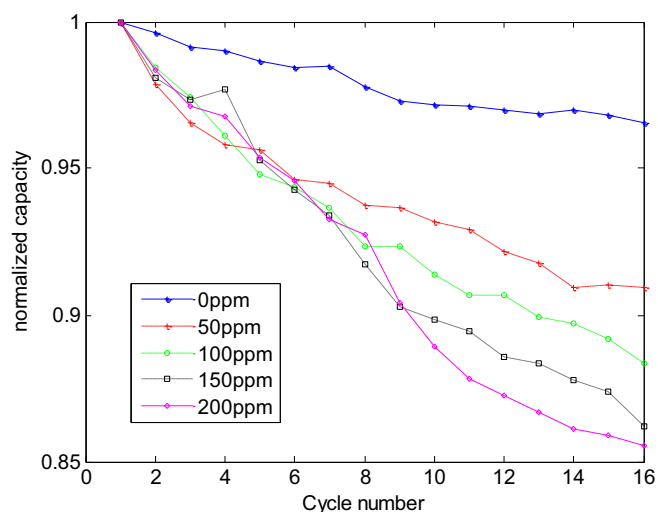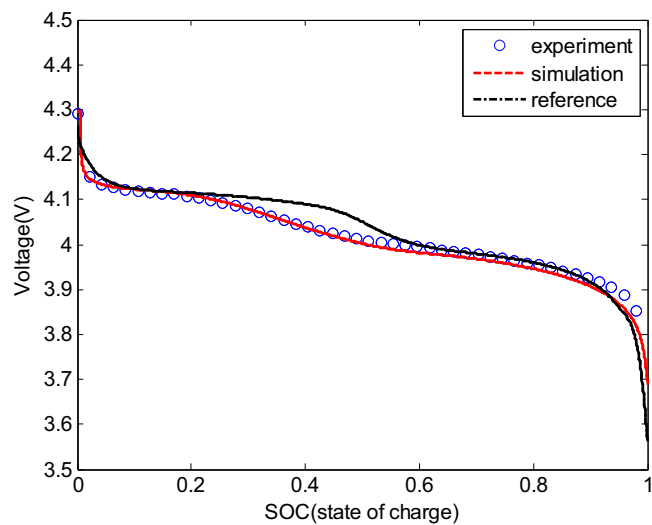
Figure 8. Capacity change with cycle number of LiMn$_2$O$_4$ electrodes with different manganese concentration in the electrolyte.

creased, which suggests that a passive cathode film layer was not fully established. The cathode electrolyte interface layer is relatively thin compared to the solid electrolyte interphase (SEI) layer of a graphite electrode, so it has less passivation effect. More capacity decrease was observed when there was a higher concentration of dissolved manganese. The low electronic conductivity of the manganese compounds formed on the cathode surface might be one reason for this lack of passivation effect. It is suggested that manganese ions dissolved from the cathode continuously form manganese compounds on the cathode surface. These manganese compounds hinder charge transfer reactions and diffusion of lithium ions, resulting in a continuous capacity fade. This result is similar to those of previous studies performed by adding manganese additives to a graphite anode. These studies also showed a continuous decrease in the capacity of the negative electrode.[15] Lithium reversibility in the graphite was found to be degraded by adding just a small amount of manganese. These reactions, in addition to loss of the cathode material, contribute to capacity fade.
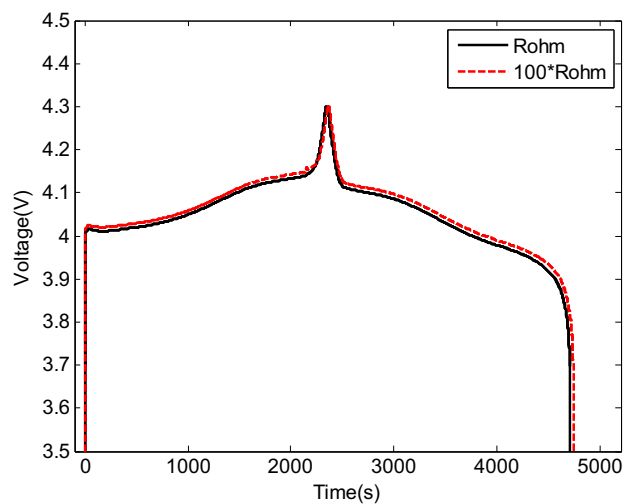
Simulation results.—Key input parameters, including open circuit voltage, electronic conductivity, discharge profile and active material dissolution rate, were measured using different experimental techniques. OCV curve and electronic conductivity were used as input to the simulation. Predicted discharge curves from simulations were compared to experiments for model validation.

Fig. 9 shows a comparison of the voltage profiles obtained by experiment and simulation. The experimentally measured OCV curve was used as input in the simulation. In Fig. 9a, the black line shows the voltage profile output using the OCV curve from a previous study[61] while the red line shows the voltage profile predicted by simulation using the measured OCV. The output voltage profile obtained in the simulation using the measured OCV curve (red line) matches the experimental result (blue circles) seamlessly. The difference between our experiment and that in the literature arises mainly from the 4.1 V plateau during discharge. The experimental OCV curve shows a voltage drop near 4.1 V mainly due to the impedance of the cell. We used our experimentally measured OCV so that we can include all cell impedance information. Fig. 9b shows the comparisons of discharge curves between experiment and simulation. The predicted discharge profile was similar to the experiment value over cycling. The model has considered the loss of active material, the increase of ohmic and charge transfer resistance, and the decrease of diffusion coefficient due to Mn dissolution.

Fig. 10 shows the simulation results of a charge and discharge cycle of the Li/LiMn$_2$O$_4$ half-cell for different values of ohmic resistance and charge transfer resistance. We can observe that higher ohmic

Capacity measurements.—The change in LiMn$_2$O$_4$ electrode capacity with cycle number with different concentration of manganese is shown in Fig. 8. The discharge capacity decreased continuously with cycles. It was obvious that higher concentrations of manganese caused greater capacity decrease. The capacity decreased significantly, up to about 15% in 16 cycles, due to dissolved Mn ions. Presumably, the deposition of manganese and electrolyte decomposition products on the electrode surface hinders the lithiation/delithiation process during cycling, which contributes to the decline of discharge capacity.[33] Moreover, the cell capacity kept decreasing as the cycle number in-

Figure 7. Effective diffusion coefficient of Li in the LiMn$_2$O$_4$ composite electrode as (a) a function of voltage and (b) a function of manganese concentration in the electrolyte.

Table V. Li diffusion coefficient with different manganese concentration in the electrolyte, measured with EIS.

Mn concentration (ppm)	Diffusion coefficient (m^2 s^{-1})
0	1.31×10^{-12}
50	5.05×10^{-13}
100	1.72×10^{-13}
150	5.31×10^{-14}
200	1.51×10^{-14}

Figure 9. (a) Comparison of voltage profile as a function of state of charge (SOC) between simulation, experiment, and data from literature.[61] (b) Comparison of discharge curve between experiment and simulation.

Figure 10. Charge and discharge voltage profile with (a) different ohmic resistance and (b) different charge transfer resistance.
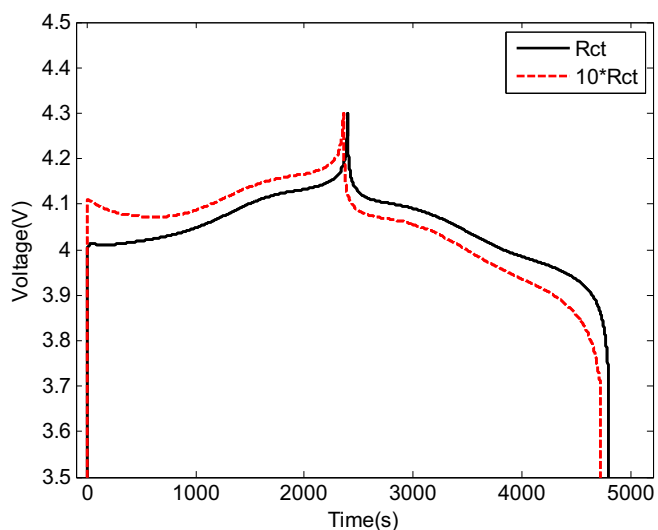
resistance mainly shifts the voltage profile higher, while higher charge transfer resistance leads to unbalance in charge and discharge curves. Since the resistance increases with the cycle number, the voltage profile changes during cycling. The increase of resistance negatively impacts capacity.

The change of volume fraction in the cathode mainly comes from Mn dissolution. As given by Eq. 52, the reaction rate constant of Mn dissolution and the concentration of H^+ are the major parameters that determine the volume fraction change. The concentration of H^+ is mainly affected by the $LiPF_6$ decomposition reaction, giving by Eq. 11.
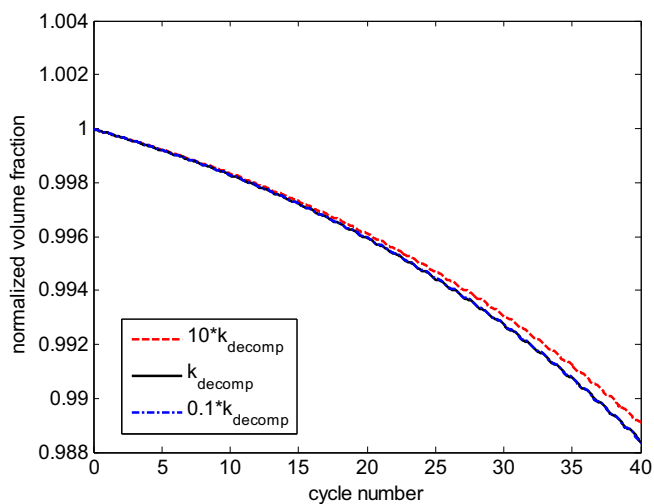
Reaction rate constant of salt decomposition was first determined by using the previous literature value. Kawamura et al. measured the reaction rate constant of different solvents with $LiPF_6$ and the order of magnitude was about 10^{-4} to 10^{-6} $(mol/l)^{-2}\,s^{-1}$, which is highly dependent on the environmental temperature.[44] We used the value of 3.56×10^{-4} $(mol/l)^{-2}\,s^{-1}$, which falls in the range. Fig. 11a shows the volume fraction of cathode material as a function of cycle number with different reaction rate constants of salt decomposition. It can be

seen that the decrease of volume fraction is not sensitive to the reaction rate of salt decomposition.

Decrease of cathode volume fraction is directly related to the reaction rate constant of Mn dissolution. Fig. 11b shows the volume fraction as a function of cycle number for different reaction rate constant of Mn dissolution. We can observe that the reaction rate constant of Mn dissolution significantly affect the volume fraction.

The effective volume fraction of the active material changes continuously due to the dissolution of manganese. A 1.87% reduction in the volume fraction of active material after 50 cycles was predicted by using a calculated reaction rate constant for manganese dissolution, as shown in Fig. 12. Similarly, the change in volume fraction of the active material from the experiment was calculated by measuring the amount of dissolved manganese ions in the electrolyte using ICP-OES. Experiments and simulations show similar trends. Previous manganese dissolution experiments based on sample weights from a powder electrode showed about 3.2% Mn dissolution.[30] Larger amounts of manganese dissolution seen in previous studies probably resulted from the use of powder electrodes, whereas a composite electrode was used for the experimental work in this study. As the cycle number increases, the volume fraction of the active material decreases and the amount of
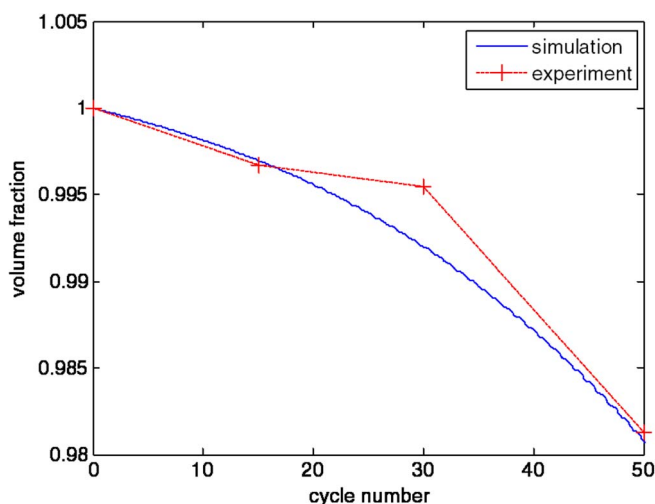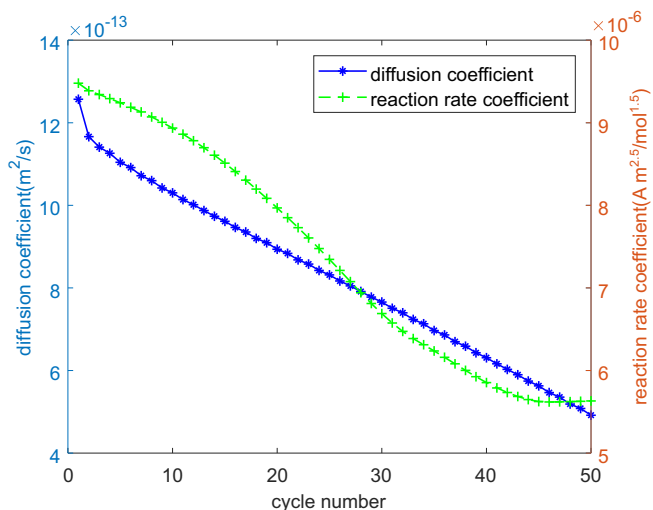
(a)
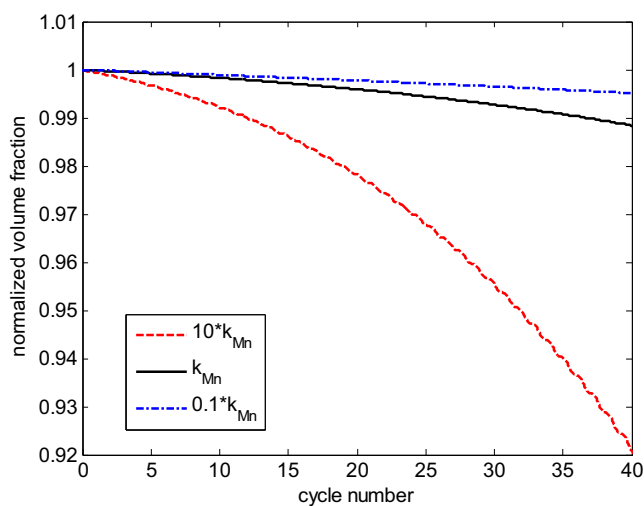
(b)

Figure 11. Volume fraction as a function of cycle number for different reaction rate constants of (a) salt decomposition and (b) Mn dissolution.

Figure 12. Comparison of simulation and experiment of volume fraction of $LiMn_2O_4$ composite electrode as a function of cycle number due to manganese dissolution.


Figure 13. Simulation shows diffusion coefficient and reaction rate coefficient as a function of cycle number.

dissolve manganese ions increases. The acceleration of these reactions results primarily from solvent oxidation, along with the generation of H_2O molecules due to the acid attack. While hydrogen ions are generated through solvent oxidation, they also react with $LiMn_2O_4$ electrodes and generate H_2O molecules that constantly regenerate HF. These reactive species continuously attack the active materials and are critical to the decrease in cell capacity.

Fig. 13 shows the changes in diffusion and reaction rate coefficients with cycle numbers from simulations. Note that the model inputs of diffusion and reaction rate coefficients are functions of Mn concentration (Table V). Therefore, along with cycling simulation and the change of Mn concentration in the electrolyte, the diffusion and reaction rate coefficients evolve with the cycle number. The diffusion coefficient of lithium ions decreases from 1.26×10^{-12} to 4.81×10^{-13} m^2 s^{-1} after 50 cycles. Experimental results showed changes of diffusion coefficient with voltage and manganese concentration (Fig. 7). The ICP results showed that approximately 55 ppm (1.016 mM) of manganese dissolved after 50 cycles. The diffusion coefficient, measured using the EIS method, decreased to 5.05×10^{-13} m^2 s^{-1} after adding 50 ppm of manganese to the electrolyte. This is consistent with our model prediction. The diffusion coefficient continuously decreases during the tested 50 cycles. Similar trends have been observed by several groups using EIS.[62–64] It was suggested that a passive layer formed on the electrode surface and clogged the pores of lithium ion path.[62] This effect continuously reduces the lithium ion diffusion coefficient.

Fig. 13 also shows that the reaction rate coefficient decreases from 9.48×10^{-6} to 5.63×10^{-6} A m$^{2.5}$ mol$^{-1.5}$ after 50 cycles. Previous experimental and computational studies have revealed a linear relationship between resistance and cycle number. Impedance measurements from a previous study[40] showed a linear increment of ohmic and electrode reaction resistance. It can be argued that a change in the contact area between the active material and the carbon black resulting from Mn dissolution is the main reason for the resistance increase. Park et al.[27] also predicted a linear increase in relative resistance with cycle number due to the manganese disproportion reaction. It is proposed that one of the main reasons for the increase in resistance comes from the loss of contact between spinel particles and the carbon conductor as the spinel dissolves into the electrolyte.

Our impedance and CV study reveal an increase in ohmic resistance, an increase in charge transfer increase, and a decrease in the reaction rate coefficient due to an increase in the concentration of manganese ions in the electrolyte. It is proposed that the growth of electrochemically generated inactive material on the surface of the cathode material contribute to this effect. Studies have shown that
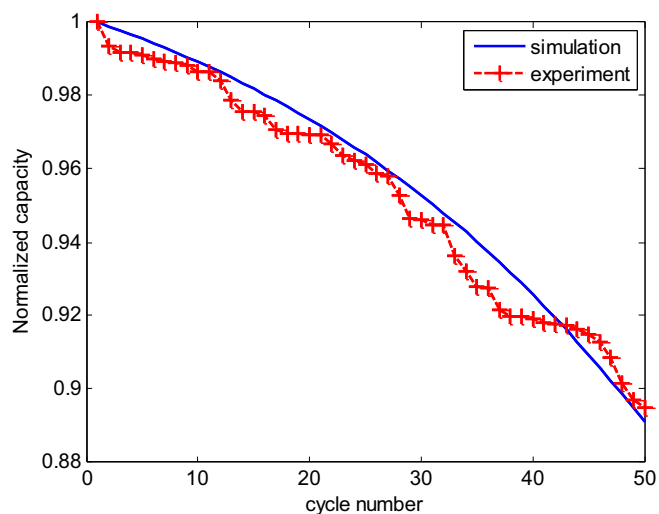
Figure 14. Comparison between simulation and experiment of normalized capacity of $LiMn_2O_4$ composite electrodes as a function of cycle number.

active material particles are covered by pristine surface films comprised primarily of Li_2CO_3 at initial cycles.[65] After repeated cycling, the electrode impedance will increase further due to the precipitation of LiF, which is derived from HF, on the surface. Additionally, Mn-F compounds generated at a later stage of storage due to manganese ions in the electrolyte aggravate electrode performance even more, by increasing resistance that leads to cell polarization.[22]

Fig. 14 shows the comparison between experiment and simulation of normalized capacity as a function of cycle number. The experiment shows approximately 10.5% capacity loss. The simulation shows about 10.9% capacity loss after 50 cycles. There have been many studies, using experiments and simulations, to describe decreases in the capacity of $LiMn_2O_4$ spinel electrodes under different conditions, such as temperature, cycle number, voltage range, preparation method, calcination temperature and surface area.[2,29,36,66–70] The range of capacity decrease also varies significantly, depending on the conditions. Previous literature has measured about 10.7%,[71] 11.03%[72] and 12%[66] decrease in capacity after 50 cycles. Our study shows an approximately 10.5% decrease in capacity, which is consistent with previous studies. Dai et al.[2] predicted 16% decrease in capacity after 50 cycles between 3.5 V and 4.3 V, at 55°C, with a C/3 rate, using a physics-based model.

Capacity loss resulting from the loss of active material in our simulation is only 1.87%. This indicates that active material loss due to manganese dissolution plays a small role. Degradations of electrode performance, such as ohmic resistance increase, charge transfer resistance increase, and diffusion coefficient decrease, are major cause of capacity decrease.

In summary, these results suggest that two key mechanisms critically impact cell performance. The first is loss of active material. The second is the increase in impedance and decrease in diffusion coefficient due to degradation of the electrode material. When cycling a battery with a cathode containing transition metal, transition metal ions can continuously dissolve from the cathode material[30] and deposit onto the positive and negative electrodes. This process not only causes a loss of active material, but also a reduction in lithium reversibility, diffusivity, conductivity and other transport properties.

The developed model can be applied to various transition metal cathodes. Studies have compared the dissolution of transition metal ions of several cathode materials,[30] showing that 3.2% of Mn ions dissolved for the $LiMn_2O_4$ cathode material whereas 0.4% of Mn ions and 0.7% of Ni ions dissolved for the $LNi_{0.5}Mn_{0.5}O_2$ cathode material. Although the degree of metal ion dissolution and degradation are different for various transition metal cathodes, the dissolution mechanism was active in all of these cases. Our model aims to account for the degradation mechanisms of cathode material due to loss of active

material, increase in impedance and decrease in diffusion coefficient. By using the developed model, the degradation of different transition metal cathodes can be predicted after measuring a few key parameters.

Conclusions

The degradation of $LiMn_2O_4$ composite electrodes and the impact on cell performance were systematically investigated in this study, using both experiments and simulations. Specifically, we focused on parameter change of the cathode due to manganese ions. Key input parameters were measured using various techniques. We also proposed an improved electrochemical model that considered side reaction and degradation of the electrode.

Electrochemical measurements were conducted by using a $LiMn_2O_4$/Li half-cell with electrolyte containing different concentrations of manganese in order to elucidate the impact of dissolved manganese on the cathode. Based on CV, EIS and cycling results, we found that manganese ions negatively impact the cathode through re-deposition. For instance, the capacity of $LiMn_2O_4$ composite electrodes decreases up to 15% after 16 cycles with 200 ppm concentration of Mn-ions dissolved in the electrolyte.

Key parameters related to battery cell performance, including surface area, electronic conductivity, impedance, and the amount of manganese dissolution, were directly measured. For instance, it was experimentally observed that 1.016 mM (55 ppm) concentration of manganese dissolved into the electrolyte after 50 cycles. The increase of ohmic resistance, decrease in diffusion coefficient due to clogging of the porous structure, and decrease in reaction rate constant due to manganese ions were calculated and used as inputs in our simulations.

The experimental observations suggest that manganese dissolution and the subsequent impact on cathode degradation should be considered in order to fully account for battery performance. A physics-based, side-reaction coupled electrochemical model with key input parameters was used to explain the magnitude and mechanisms of electrode degradation. The simulations and experiments showed capacity decrease of 10.9% and 10.5% after 50 cycles, respectively, due to side reactions. Our studies suggest that loss of active material and parameter change due to degradation are key factors that affect cell performance. Decline in lithium reversibility, diffusivity, conductivity and other transport properties are the most significant cause of cathode degradation.

Appendix

Electronic conductivity measurement –Four point probe method.— Potential difference is measured from the inner two probes while the current is supplied and extracted from the outer two probes. The electronic conductivity of the composite electrode is calculated as

$$\kappa_s^{eff} = \frac{\ln(2)}{\pi t_e}\left(\frac{I}{E}\right) = \frac{0.221}{t_e}\left(\frac{I}{E}\right)$$

where t_e is the electrode thickness, κ_s^{eff} is the electronic conductivity of the electrode, I is the applied current and E is the electric potential difference between two probes.

List of Symbols

a_s	specific surface area of positive electrode, m^{-1}
$a_{s,oxide}$	specific surface area for solvent oxidation reaction, m^{-1}
$brug$	Bruggemann coefficient
c_1	concentration of lithium ions in the solid phase, mol m^{-3}
c_i	concentration of species i in the electrolyte (i = Li$^+$, Mn^{2+}, H$^+$, H$_2$O), mol m^{-3}

$c_{1,0}$	initial concentration of lithium ions in the solid phase, mol m^{-3}
$c_{1,max}$	maximum solid phase concentration, mol m^{-3}
$c_{1,max0}$	initial maximum solid phase concentration, mol m^{-3}
$c_{1,surf}$	lithium concentration at particle surface, mol m^{-3}
D_1	diffusivity of lithium ion in solid, m^2 s^{-1}
$D_{1,0}$	initial diffusivity of lithium ion in solid, m^2 s^{-1}
D_i	diffusivity of species i in the electrolyte (i = Li$^+$, Mn^{2+}, H$^+$, H$_2$O), m^2 s^{-1}
D_i^{eff}	effective diffusivity of species i in the electrolyte (i = Li$^+$, Mn^{2+}, H$^+$, H$_2$O), m^2 s^{-1}
E_{OCV}	open circuit potential, V
$f_{\pm}$	electrolyte activity coefficient
F	Faraday's constant, C mol^{-1}
i_{0,Li^+}	exchange current density of lithium intercalation/deintercalation at cathode, A m^{-2}
$i_{0,oxid}$	exchange current density of solvent oxidation at cathode, A m^{-2}
i_{H_dep}	current density of hydrogen deposition at lithium metal anode, A m^{-2}
i_{Li^+}	current density of lithium intercalation/deintercalation at cathode, A m^{-2}
$i_{Li^+,metal}$	current density of lithium reaction at lithium metal anode, A m^{-2}
i_{Mn_dep}	current density of Mn deposition at lithium metal anode, A m^{-2}
i_{Mn_redep}	current density of Mn re-deposition at cathode, A m^{-2}
i_{oxid}	current density of solvent oxidation at cathode, A m^{-2}
i_{tot}	sum of all the current density at cathode, A m^{-2}
I_{app}	applied current density, A m^{-2}
k_{decomp}	reaction rate constant of salt decomposition, m^6 mol^{-2} s^{-1}
k_{H_dep}	reaction rate constant of hydrogen deposition at lithium metal anode, A m mol^{-1}
k_{Li^+}	reaction rate constant of lithium at cathode, A m$^{2.5}$ mol$^{-1.5}$
$k_{Li^+,metal}$	reaction rate constant of lithium at lithium metal anode, A m$^{-0.5}$ mol$^{-0.5}$
k_{Mn_dep}	reaction rate constant of Mn deposition at lithium metal anode, A m mol^{-1}
k_{Mn_dis}	reaction rate constant of Mn dissolution due to acid attack, m s^{-1}
k_{Mn_redep}	reaction rate constant of Mn re-deposition at cathode, A m mol^{-1}
L_{pos}	cathode thickness, m
L_{sep}	separator thickness, m
n_1	adjustment factor of lithium diffusivity
r	radial coordinate, m
r_s	particle radius, m
R	universal gas constant, J mol^{-1} K^{-1}
R_{ct}	charge transfer resistance of the electrode, Ω m^2
R_{decomp}	reaction rate of salt decomposition, mol m^{-3} s^{-1}
R_{Mn_dis}	reaction rate of Mn dissolution due to acid attack, mol m^{-2} s^{-1}
R_{Mn_redep}	reaction rate of Mn re-deposition at cathode, mol m^{-2} s^{-1}
R_{ohmic}	ohmic resistance of the electrode, Ω m^2
R_{oxid}	reaction rate of solvent oxidation at cathode, mol m^{-2} s^{-1}
S	cathode surface area, m^2
t_+^0	lithium ion transference number
T	temperature, K
U_{H_dep}	equilibrium potential of hydrogen deposition, V
U_{Li^+}	equilibrium potential of lithium intercalation/deintercalation reaction, V
U_{Mn_dep}	equilibrium potential of Mn deposition, V
U_{Mn_redep}	equilibrium potential of Mn re-deposition, V
U_{oxid}	equilibrium potential of solvent oxidation, V
V_{LMO}	molar volume of cathode active material, m^3 mol^{-1}
V_M	molar volume of cathode, m^3 mol^{-1}
x	coordinate along the electrode thickness, m
Z	Warburg impedance

Greek

$\alpha_{a,Li}$	anodic transfer coefficient of lithium intercalation/deintercalation reaction
$\alpha_{a,Li}^{metal}$	anodic transfer coefficient at lithium metal anode
$\alpha_{a,oxid}$	anodic transfer coefficient of solvent oxidation
α_{c,H_dep}	cathodic transfer coefficient of hydrogen deposition
$\alpha_{c,Li}$	cathodic transfer coefficient of lithium intercalation/deintercalation reaction
$\alpha_{c,Li}^{metal}$	cathodic transfer coefficient at lithium metal anode
α_{c,Mn_dep}	cathodic transfer coefficient of Mn deposition
α_{c,Mn_redep}	cathodic transfer coefficient of Mn re-deposition
δ	Warburg prefactor
ε_1	volume fraction of electrode active material
$\varepsilon_{1,0}$	initial volume fraction of electrode active material
ε_2	volume fraction of electrolyte
η_{Li^+}	overpotential for lithium intercalation/deintercalation reaction, V
η_{oxid}	overpotential of the solvent oxidation reaction, V
κ_1^{eff}	effective solid phase electronic conductivity, S m^{-1}
κ_2	bulk electrolyte phase conductivity, S m^{-1}

κ_2^{eff}	effective electrolyte phase conductivity, S m^{-1}
ϕ_1	solid phase potential, V
ϕ_2	electrolyte phase potential, V
ϕ_{Li_metal}	potential at lithium metal anode, V
ω	angular frequency, rad s^{-1}
y	intercalation level

ORCID

Yoon Koo Lee https://orcid.org/0000-0001-9383-8467
Jonghyun Park https://orcid.org/0000-0003-4241-3842
Wei Lu https://orcid.org/0000-0002-4851-1032

References

1. P. Arora, R. E. White, and M. Doyle, *J. Electrochem. Soc.*, **145**, 3647 (1998).
2. Y. Dai, L. Cai, and R. E. White, *J. Electrochem. Soc.*, **160**, A182 (2013).
3. J. Vetter, P. Novak, M. R. Wagner, C. Veit, K. C. Möller, J. O. Besenhard, M. Winter, M. Wohlfahrt-Mehrens, C. Vogler, and A. Hammouche, *J. Power Sources*, **147**, 269 (2005).
4. D. Zhang, B. S. Haran, A. Durairajan, R. E. White, Y. Podrazhansky, and B. N. Popov, *J. Power Sources*, **91**, 122 (2000).
5. Y. K. Lee, J. Park, and W. Lu, *J. Electrochem. Soc.*, **163**, A1359 (2016).
6. J. Shim, R. Kostecki, T. Richardson, X. Song, and K. A. Striebel, *J. Power Sources*, **112**, 222 (2002).
7. L. Yang, M. Takahashi, and B. Wang, *Electrochim. Acta*, **51**, 3228 (2006).
8. D. H. Jang and S. M. Oh, *J. Electrochem. Soc.*, **144**, 3342 (1997).
9. R. J. Gummow, A. de Kock, and M. M. Thackeray, *Solid State Ionics*, **69**, 59 (1994).
10. E. Iwata, K.-I. Takahashi, K. Maeda, and T. Mouri, *J. Power Sources*, **81–82**, 430 (1999).
11. D. P. Abraham, T. Spila, M. M. Furczon, and E. Sammann, *Electrochem. Solid-State Lett.*, **11**, A226 (2008).
12. A. Biyr and C. Sigala, *J Eletrochem Soc*, **145**, 194 (1998).
13. C. Delacourt, A. Kwong, X. Liu, R. Qiao, W. L. Yang, P. Lu, S. J. Harris, and V. Srinivasan, *J. Electrochem. Soc.*, **160**, A1099 (2013).
14. S. Komaba, T. Itabashi, T. Ohtsuka, H. Groult, N. Kumagai, B. Kaplan, and H. Yashiro, *J. Electrochem. Soc.*, **152**, A937 (2005).
15. S. Komaba, N. Kumagai, and Y. Kataoka, *Electrochim. Acta*, **47**, 1229 (2002).
16. M. Ochida, T. Doi, Y. Domi, S. Tsubouchi, H. Nakagawa, T. Yamanaka, T. Abe, and Z. Ogumi, *J. Electrochem. Soc.*, **160**, A410 (2013).
17. M. Ochida, Y. Domi, T. Doi, S. Tsubouchi, H. Nakagawa, T. Yamanaka, T. Abe, and Z. Ogumi, *J. Electrochem. Soc.*, **159**, A961 (2012).
18. H. Shin, J. Park, A. M. Sastry, and W. Lu, *J. Power Sources*, **284**, 416 (2015).
19. T. Tsujikawa, K. Yabuta, T. Matsushita, M. Arakawa, and K. Hayashi, *ECS Trans.*, **25**, 309 (2010).
20. H. Tsunekawa, S. Tanimoto, R. Marubayashi, M. Fujita, K. Kifune, and M. Sano, *J. Electrochem. Soc.*, **149**, A1326 (2002).
21. C. Zhan, J. Lu, A. J. Kropf, T. Wu, A. N. Jansen, Y.-K. Sun, X. Qiu, and K. Amine, *Nat. Commun.*, **4** (2013).
22. D. Kim, S. Park, O. B. Chae, J. H. Ryu, Y.-U. Kim, R.-Z. Yin, and S. M. Oh, *J. Electrochem. Soc.*, **159**, A193 (2012).
23. K. Edström, T. Gustafsson, and J. O. Thomas, *Electrochim. Acta*, **50**, 397 (2004).
24. J. Lei, L. Li, R. Kostecki, R. Muller, and F. McLarnon, *J. Electrochem. Soc.*, **152**, A774 (2005).
25. M. Matsui, K. Dokko, and K. Kanamura, *J. Electrochem. Soc.*, **157**, A121 (2010).
26. Y. Matsuo, R. Kostecki, and F. McLarnon, *J. Electrochem. Soc.*, **148**, A687 (2001).
27. J. Park, J. H. Seo, G. Plett, W. Lu, and A. M. Sastry, *Electrochem. Solid-State Lett.*, **14**, A14 (2011).
28. C.-H. Lu and S.-W. Lin, *J. Mater. Res.*, **17**, 1476 (2002).
29. X. Lin, J. Park, L. Liu, Y. Lee, A. M. Sastry, and W. Lu, *J. Electrochem. Soc.*, **160**, A1701 (2013).
30. W. Choi and A. Manthiram, *J. Electrochem. Soc.*, **153**, A1760 (2006).
31. K. G. Gallagher, S. E. Trask, C. Bauer, T. Woehrle, S. F. Lux, M. Tschech, P. Lamp, B. J. Polzin, S. Ha, B. Long, Q. L. Wu, W. Q. Lu, D. W. Dees, and A. N. Jansen, *J. Electrochem. Soc.*, **163**, A138 (2016).
32. K. Amine, J. Liu, S. Kang, I. Belharouak, Y. Hyung, D. Vissers, and G. Henriksen, *J. Power Sources*, **129**, 14 (2004).
33. Y. K. Lee, J. Park, and W. Lu, *J. Electrochem. Soc.*, **164**, A2812 (2017).
34. T. Inoue and M. Sano, *J. Electrochem. Soc.*, **145**, 3704 (1998).
35. L.-F. Wang, C.-C. Ou, K. A. Striebel, and J.-S. Chen, *J. Electrochem. Soc.*, **150**, A905 (2003).
36. Y. Xia, Y. Zhou, and M. Yoshio, *J. Electrochem. Soc.*, **144**, 2593 (1997).
37. B. J. Johnson, D. H. Doughty, J. A. Voigt, and T. J. Boyle, *J. Power Sources*, **68**, 634 (1997).
38. R. Benedek and M. M. Thackeray, *Electrochem. Solid-State Lett.*, **9**, A265 (2006).
39. A. Du Pasquier, A. Blyr, P. Courjal, D. Larcher, G. Amatucci, B. Gérand, and J. M. Tarascon, *J. Electrochem. Soc.*, **146**, 428 (1999).
40. E. Wang, D. Ofer, W. Bowden, N. Iltchev, R. Moses, and K. Brandt, *J. Electrochem. Soc.*, **147**, 4023 (2000).
41. D. H. Jang, Y. J. Shin, and S. M. Oh, *J. Electrochem. Soc.*, **143**, 2204 (1996).
42. R. Darling and J. Newman, *J. Electrochem. Soc.*, **145**, 990 (1998).

43. C. G. Barlowz, *Electrochem. Solid-State Lett.*, **2**, 362 (1999).
44. T. Kawamura, S. Okada, and J.-i. Yamaki, *J. Power Sources*, **156**, 547 (2006).
45. Y. Xia and M. Yoshio, *J. Electrochem. Soc.*, **143**, 825 (1996).
46. D. Aurbach, B. Markovsky, I. Weissman, E. Levi, and Y. Ein-Eli, *Electrochim. Acta*, **45**, 67 (1999).
47. M. A. Monem, K. Trad, N. Omar, O. Hegazy, B. Mantels, G. Mulder, P. Van den Bossche, and J. Van Mierlo, *Appl Energ*, **152**, 143 (2015).
48. M. Schoenleber, C. Uhlmann, P. Braun, A. Weber, and E. Ivers-Tiffee, *Electrochim. Acta*, **243**, 250 (2017).
49. W. Waag, S. Kabitz, and D. U. Sauer, *Appl Energ*, **102**, 885 (2013).
50. P. Arora, M. Doyle, and R. E. White, *J. Electrochem. Soc.*, **146**, 3543 (1999).
51. W. Fang, O. J. Kwon, and C.-Y. Wang, *Int. J. Energy Res.*, **34**, 107 (2010).
52. P. Ramadass, B. Haran, R. White, and B. N. Popov, *J. Power Sources*, **123**, 230 (2003).
53. M. D. Levi, K. Gamolsky, D. Aurbach, U. Heider, and R. Oesten, *Electrochim. Acta*, **45**, 1781 (2000).
54. Q.-C. Zhuang, S. Xu, X. Qiu, Y. Cui, L. Fang, and S. Sun, *Prog. Chem.*, **22**, 1044 (2010).
55. G. Sikha, B. N. Popov, and R. E. White, *J. Electrochem. Soc.*, **151**, A1104 (2004).
56. J. F. Yan, T. V. Nguyen, R. E. White, and R. B. Griffin, *J. Electrochem. Soc.*, **140**, 733 (1993).
57. J. Marzec, K. Świerczek, J. Przewoźnik, J. Molenda, D. R. Simon, E. M. Kelder, and J. Schoonman, *Solid State Ionics*, **146**, 225 (2002).
58. J. Molenda and W. Kucza, *Solid State Ionics*, **117**, 41 (1999).
59. M. Park, X. Zhang, M. Chung, G. B. Less, and A. M. Sastry, *J. Power Sources*, **195**, 7904 (2010).
60. S. Lim and J. Cho, *Electrochem. Commun.*, **10**, 1478 (2008).
61. M. Doyle, J. Newman, A. S. Gozdz, C. N. Schmutz, and J. M. Tarascon, *J. Electrochem. Soc.*, **143**, 1890 (1996).
62. S. R. Das, S. B. Majumder, and R. S. Katiyar, *J. Power Sources*, **139**, 261 (2005).
63. K. A. Striebel, A. Rougier, C. R. Horne, R. P. Reade, and E. J. Cairns, *J. Electrochem. Soc.*, **146**, 4339 (1999).
64. D. Zhang, B. N. Popov, and R. E. White, *J. Power Sources*, **76**, 81 (1998).
65. D. Aurbach, K. Gamolsky, B. Markovsky, G. Salitra, Y. Gofer, U. Heider, R. Oesten, and M. Schmidt, *J. Electrochem. Soc.*, **147**, 1322 (2000).
66. C.-H. Doh, J.-H. Lee, D.-J. Lee, B.-S. Jin, and S.-I. Moon, *Bull. Korean Chem. Soc.*, **30**, 2429 (2009).
67. M. Y. Song, D. S. Ahn, and H. R. Park, *J. Power Sources*, **83**, 57 (1999).
68. Y.-K. Sun, I.-H. Oh, and K. Y. Kim, *Ind. Eng. Chem. Res.*, **36**, 4839 (1997).
69. Y. Xia, N. Kumada, and M. Yoshio, *J. Power Sources*, **90**, 135 (2000).
70. X. Xiao, J. Lu, and Y. Li, *Nano Res.*, **3**, 733 (2010).
71. L. Xiong, Y. Xu, C. Zhang, Z. Zhang, and J. Li, *J Solid State Electrochem*, **15**, 1263 (2011).
72. Y.-K. Sun and S.-H. Jin, *J. Mater. Chem.*, **8**, 2399 (1998).